

# The Complex Organic Molecules of Embedded Protostars at Perseus

YAO-LUN YANG,<sup>1,2</sup> NAMI SAKAI,<sup>2</sup> AND YICHEN ZHANG<sup>2</sup>

<sup>1</sup>*Department of Astronomy, University of Virginia, Charlottesville, VA 22904-4235, USA*

<sup>2</sup>*RIKEN Cluster for Pioneering Research, Wako-shi, Saitama, 351-0106, Japan*

## 1. INTRODUCTION

Planet formation may start during the embedded phase of star formation. In the scenario where planets form from the embedded disks, resulting in substructures, the chemistry of embedded disks may play a significant role for the chemical composition of the forming planets. In the recent years, observations discover the emission of carbon-chain molecules and complex organic molecules (COMs) toward the center of several embedded protostars, indicating that embedded protostars have developed a complex chemistry at the disk-forming region. If the forming planets inherit the chemistry of embedded disks, the abundance of complex organic molecules may implicate future developments of organics on the planets.

Heavier or more complex molecules, such as cyclic-C<sub>3</sub>H<sub>2</sub>, SO, and complex organic molecules (COMs), are in the gas phase at the inner protostellar envelope ( $T \gtrsim 100$  K), exclusively tracing the properties of the inner envelope where a disk may be forming (Aikawa 2013; Sakai et al. 2014). The kinematics of a rotating infalling envelope has been analyzed with the observations of heavier or more complex molecules, such as CH<sub>3</sub>OH and CH<sub>2</sub>DOH for HH 212 (Lee et al. 2017), CS for IRAS 04365+2535 (Sakai et al. 2016) and L483 (Oya et al. 2017), cyclic-C<sub>3</sub>H<sub>2</sub> for L1527 (Sakai et al. 2014), OCS for IRAS 16293–2422 A (Oya et al. 2016), and methanol and HCOOH for B335 (Imai et al. 2019).

In the review by Herbst & van Dishoeck (2009), complex molecules are defined as carbon-bearing molecules that contain six atoms or more. Saturated complex molecules are rich in hydrogen atoms, often called complex organic molecules (COMs), while the unsaturated complex molecules are lack of hydrogen atoms, mostly in the form of long carbon-chain molecules. While recent observations show several embedded protostars with rich spectra of complex molecules, the occurrence of complex molecules at embedded protostars and its relation-

ship to the star formation process remain poorly understood. Several protostars are rich in COMs but show little emission of long carbon-chain molecules, such as IRAS 16293–2422 (Jørgensen et al. 2016), NGC 1333 IRAS 4A (Bottinelli et al. 2004), B335 (Imai et al. 2016, 2019), and BHR 71 (Yang et al. 2020 accepted); some protostars are rich in long carbon-chain molecules but not in COMs, such as L1527 (Sakai et al. 2010) and IRAS 15398–3359 (Sakai et al. 2009). While the bimodal chemical appearance hints a bimodal evolutionary path, the chemical evolution at the embedded protostars remain ill-constrained as a few protostars show the emission of both COMs and long carbon-chain molecules at different scales, such as L483 (Oya et al. 2017).

The Perseus ALMA Chemistry Survey (PEACHES) aims to provide the statistics on the occurrence of complex molecules at embedded protostars. This program unbiasedly observes 51 embedded protostars with ALMA around 260 GHz, covering the emission of simple molecules such as CS and H<sup>13</sup>CN as well as the emission of complex molecules including CH<sub>3</sub>OH and CH<sub>3</sub>OCHO.

## 2. OBSERVATIONS

Set3 has the continuum window ranging from 245800 MHz to 246730 MHz, while the Set1 and Set1 have the continuum window ranging from 246200 MHz to 247130 MHz.

## 3. RESULTS

The ALMA image cubes are post-processed to extract 1D spectra for identifying the emission of complex molecules and more in-depth analyses. Because the complex molecules only sublime at the temperature greater than  $\sim 100$  K, we focus on the spectra toward the continuum sources. Our steps of post-processing reduces the image cubes to 1D spectra, which are summarized below.

- **Continuum fitting:** We use the CASA task `imfit` to iteratively fit for continuum sources down to  $5\sigma$  of the residual image within the central 70% of the primary beam size ( $20''$ ). For Set3-ID09, the fitting uses a threshold of  $4\sigma$  and extends the

**Table 1.** PEACHES Sample

Source	Common names	R.A. (J2000)	Decl. (J2000)	$v_{\text{lsr}}$	Beam	Cont. Size	$T_{\text{cont}}$	Ref. ( $v_{\text{lsr}}$ )
		(hh:mm:ss)	(dd:mm:ss)	(km s <sup>-1</sup> )	( $''$ )	( $''$ )	(K)	
Per-emb 22 B		03:25:22.35	30:45:13.11	4.3	$0''.64 \times 0''.39$	$0''.95 \times 0''.51$	0.92	S19
Per-emb 22 A		03:25:22.41	30:45:13.26	4.3	$0''.64 \times 0''.39$	$0''.86 \times 0''.65$	1.71	S19
L1448 NW	L1448 IRS 3C	03:25:35.67	30:45:34.16	4.2	$0''.64 \times 0''.39$	$0''.83 \times 0''.47$	3.15	H18
Per-emb 33 B/C		03:25:36.32	30:45:15.19	5.3	$0''.64 \times 0''.39$	$0''.75 \times 0''.48$	5.55	S19
Per-emb 33 A		03:25:36.38	30:45:14.72	5.3	$0''.64 \times 0''.39$	$0''.73 \times 0''.45$	10.33	S19
L1448 IRS 3A		03:25:36.50	30:45:21.90	4.6	$0''.64 \times 0''.39$	$0''.85 \times 0''.59$	3.21	H18
Per-emb 26		03:25:38.88	30:44:05.28	5.4	$0''.64 \times 0''.39$	$0''.69 \times 0''.45$	8.03	S19
Per-emb 42		03:25:39.14	30:43:57.90	5.8	$0''.64 \times 0''.39$	$0''.64 \times 0''.39$	0.66	S19
Per-emb 25	IRAS 03235+3004	03:26:37.51	30:15:27.81	5.5	$0''.64 \times 0''.39$	$0''.69 \times 0''.41$	5.27	S18
Per-emb 17	L1455 IRS 1, IRAS 03245+3002	03:27:39.11	30:13:02.96	6.0	$0''.64 \times 0''.40$	$0''.79 \times 0''.48$	2.00	S19
Per-emb 20	L1455 IRS 4	03:27:43.28	30:12:28.88	5.3	$0''.64 \times 0''.40$	$1''.29 \times 0''.78$	0.14	S19
L1455 IRS 2		03:27:47.69	30:12:04.33	5.1	$0''.64 \times 0''.40$	$0''.60 \times 0''.38$	0.13	H18
Per-emb 35 A	NGC 1333 IRAS 1	03:28:37.10	31:13:30.77	7.4	$0''.66 \times 0''.42$	$0''.75 \times 0''.51$	0.93	Y20
Per-emb 35 B	NGC 1333 IRAS 1	03:28:37.22	31:13:31.74	7.3	$0''.66 \times 0''.42$	$0''.78 \times 0''.53$	0.75	Y20
Per-emb 27	NGC 1333 IRAS 2A	03:28:55.57	31:14:36.97	6.5	$0''.66 \times 0''.42$	$0''.93 \times 0''.66$	5.79	Y20
EDJ2009-172		03:28:56.65	31:18:35.43	...	$0''.66 \times 0''.42$	$0''.69 \times 0''.44$	0.62	...
Per-emb 36	NGC 1333 IRAS 2B	03:28:57.37	31:14:15.77	6.9	$0''.66 \times 0''.42$	$0''.73 \times 0''.46$	5.56	S19
Per-emb 54	NGC 1333 IRAS 6	03:29:01.55	31:20:20.49	7.9	$0''.66 \times 0''.42$	$0''.69 \times 0''.40$	0.07	S19
SVS 13B	NGC 1333 SVS 13B	03:29:03.08	31:15:51.73	8.5	$0''.66 \times 0''.42$	$0''.87 \times 0''.68$	6.64	S19
SVS 13A2	VLA 3	03:29:03.39	31:16:01.58	8.4	$0''.66 \times 0''.42$	$0''.86 \times 0''.53$	0.61	S18
Per-emb 44	NGC 1333 SVS 13A	03:29:03.76	31:16:03.70	8.7	$0''.66 \times 0''.42$	$0''.98 \times 0''.79$	6.84	S19
Per-emb 15		03:29:04.06	31:14:46.23	6.8	$0''.66 \times 0''.42$	$0''.89 \times 0''.70$	0.17	S19
Per-emb 50	IRAS 03260+3111 A	03:29:07.77	31:21:57.11	9.3	$0''.66 \times 0''.42$	$0''.73 \times 0''.44$	4.13	Y20
Per-emb 12 B	NGC 1333 IRAS 4A2	03:29:10.44	31:13:32.08	6.9	$0''.66 \times 0''.42$	$1''.33 \times 0''.81$	10.04	S19
Per-emb 12 A	NGC 1333 IRAS 4A1	03:29:10.54	31:13:30.93	6.9	$0''.66 \times 0''.42$	$1''.11 \times 0''.98$	21.85	S19
Per-emb 21	NGC 1333 IRAS 7 SM2	03:29:10.67	31:18:20.16	8.6	$0''.66 \times 0''.42$	$0''.74 \times 0''.48$	2.05	Y20
Per-emb 18	NGC 1333 IRAS 7 SM1	03:29:11.27	31:18:31.09	8.1	$0''.66 \times 0''.42$	$0''.84 \times 0''.73$	3.42	S19
Per-emb 13	NGC 1333 IRAS 4B1	03:29:12.02	31:13:07.99	7.1	$0''.66 \times 0''.42$	$1''.07 \times 0''.83$	14.76	S19
IRAS4B'	NGC 1333 IRAS 4B2	03:29:12.85	31:13:06.87	7.1	$0''.66 \times 0''.42$	$0''.83 \times 0''.74$	7.13	S19
Per-emb 14	NGC 1333 IRAS 4C	03:29:13.55	31:13:58.12	7.9	$0''.66 \times 0''.42$	$0''.79 \times 0''.50$	3.05	S19
EDJ2009-235		03:29:18.26	31:23:19.73	7.7	$0''.67 \times 0''.42$	$0''.66 \times 0''.44$	0.26	Y20
EDJ2009-237		03:29:18.74	31:23:25.24	...	$0''.67 \times 0''.42$	$0''.67 \times 0''.42$	0.12	...
Per-emb 37		03:29:18.97	31:23:14.28	7.5	$0''.67 \times 0''.42$	$0''.82 \times 0''.57$	0.56	Y20
Per-emb 60		03:29:20.05	31:24:07.35	...	$0''.67 \times 0''.42$	$0''.73 \times 0''.47$	0.08	...
Per-emb 5	IRAS 03282+3035	03:31:20.94	30:45:30.24	7.3	$0''.45 \times 0''.30$	$0''.56 \times 0''.41$	15.29	S19
Per-emb 2	IRAS 03292+3039	03:32:17.92	30:49:47.81	7.0	$0''.45 \times 0''.30$	$1''.35 \times 0''.97$	7.41	S19
Per-emb 10	B1-d	03:33:16.43	31:06:52.01	6.4	$0''.46 \times 0''.30$	$0''.49 \times 0''.32$	1.82	S19
Per-emb 40	B1-a	03:33:16.67	31:07:54.87	7.4	$0''.46 \times 0''.30$	$0''.47 \times 0''.32$	1.44	S19
Per-emb 29	B1-c	03:33:17.88	31:09:31.74	6.1	$0''.46 \times 0''.30$	$0''.56 \times 0''.39$	8.41	Y20
B1-b N		03:33:21.21	31:07:43.63	6.6	$0''.46 \times 0''.30$	$0''.56 \times 0''.47$	7.67	C16
B1-b S		03:33:21.36	31:07:26.34	6.6	$0''.46 \times 0''.30$	$0''.63 \times 0''.53$	14.79	C16
Per-emb 16		03:43:50.97	32:03:24.12	8.8	$0''.50 \times 0''.32$	$0''.61 \times 0''.52$	0.35	S19
Per-emb 28		03:43:51.01	32:03:08.02	8.6	$0''.50 \times 0''.32$	$0''.56 \times 0''.32$	1.52	S19
Per-emb 1	HH 211 MMS	03:43:56.81	32:00:50.16	9.4	$0''.49 \times 0''.32$	$0''.68 \times 0''.48$	4.57	S19
Per-emb 11 B	IC 348 MMS	03:43:56.88	32:03:03.08	9.0	$0''.50 \times 0''.33$	$0''.92 \times 0''.69$	0.40	S19
Per-emb 11 A	IC 348 MMS	03:43:57.07	32:03:04.76	9.0	$0''.50 \times 0''.33$	$0''.61 \times 0''.48$	10.47	S19
Per-emb 11 C	IC 348 MMS	03:43:57.70	32:03:09.82	9.0	$0''.50 \times 0''.33$	$1''.10 \times 0''.86$	0.34	S19
Per-emb 55	IRAS 03415+3152	03:44:43.30	32:01:31.22	12.0	$0''.50 \times 0''.32$	$0''.49 \times 0''.33$	0.32	S19
Per-emb 8		03:44:43.98	32:01:35.19	11.0	$0''.50 \times 0''.32$	$0''.49 \times 0''.36$	8.51	S19
Per-emb 53	B5 IRS 1	03:47:41.59	32:51:43.62	10.2	$0''.51 \times 0''.33$	$0''.58 \times 0''.42$	1.55	Y20

**References**—C16=Carney et al. (2016); H18=Higuchi et al. (2018); S18=Stephens et al. (2018); S19=Stephens et al. (2019); Y20=this study.

Table 2. PEACHES Sample

PEACHES ID	Source	Common names	R.A. (J2000)	Decl. (J2000)	$v_{\text{lsr}}$	Beam	Cont. Size	$T_{\text{cont}}$	Ref. ( $v_{\text{lsr}}$ )
			(hh:mm:ss)	(dd:mm:ss)	(km s <sup>-1</sup> )	( $''$ )	( $''$ )	(K)	
Set1_ID00	L1448 NW	L1448 IRS 3C	03:25:35.67	30:45:34.16	4.2	0 $''$ 64×0 $''$ 39	0 $''$ 83×0 $''$ 47	3.15	H18
Set1_ID01.3	Per-emb 33 A		03:25:36.38	30:45:14.72	5.3	0 $''$ 64×0 $''$ 39	0 $''$ 73×0 $''$ 45	10.33	S19
Set1_ID01.4	Per-emb 33 B/C		03:25:36.32	30:45:15.19	5.3	0 $''$ 64×0 $''$ 39	0 $''$ 75×0 $''$ 48	5.55	S19
Set1_ID01.2	L1448 IRS 3A		03:25:36.50	30:45:21.90	4.6	0 $''$ 64×0 $''$ 39	0 $''$ 85×0 $''$ 59	3.21	H18
Set1_ID02	Per-emb 26		03:25:38.88	30:44:05.28	5.4	0 $''$ 64×0 $''$ 39	0 $''$ 69×0 $''$ 45	8.03	S19
Set1_ID02.2	Per-emb 42		03:25:39.14	30:43:57.90	5.8	0 $''$ 64×0 $''$ 39	0 $''$ 64×0 $''$ 39	0.66	S19
Set1_ID03	Per-emb 22 A		03:25:22.41	30:45:13.26	4.3	0 $''$ 64×0 $''$ 39	0 $''$ 86×0 $''$ 65	1.71	S19
Set1_ID03.2	Per-emb 22 B		03:25:22.35	30:45:13.11	4.3	0 $''$ 64×0 $''$ 39	0 $''$ 95×0 $''$ 51	0.92	S19
Set1_ID05	Per-emb 25	IRAS 03235+3004	03:26:37.51	30:15:27.81	5.5	0 $''$ 64×0 $''$ 39	0 $''$ 69×0 $''$ 41	5.27	S18
Set1_ID06	Per-emb 17	L1455 IRS 1, IRAS 03245+3002	03:27:39.11	30:13:02.96	6.0	0 $''$ 64×0 $''$ 40	0 $''$ 79×0 $''$ 48	2.00	S19
Set1_ID07	Per-emb 20	L1455 IRS 4	03:27:43.28	30:12:28.88	5.3	0 $''$ 64×0 $''$ 40	1 $''$ 29×0 $''$ 78	0.14	S19
Set1_ID08	L1455 IRS 2		03:27:47.69	30:12:04.33	5.1	0 $''$ 64×0 $''$ 40	0 $''$ 60×0 $''$ 38	0.13	H18
Set2_ID00	Per-emb 44	NGC 1333 SVS 13A	03:29:03.76	31:16:03.70	8.7	0 $''$ 66×0 $''$ 42	0 $''$ 98×0 $''$ 79	6.84	S19
Set2_ID00.2	SVS 13A2	VLA 3	03:29:03.39	31:16:01.58	8.4	0 $''$ 66×0 $''$ 42	0 $''$ 86×0 $''$ 53	0.61	S18
Set2_ID01	Per-emb 12 A	NGC 1333 IRAS 4A1	03:29:10.54	31:13:30.93	6.9	0 $''$ 66×0 $''$ 42	1 $''$ 11×0 $''$ 98	21.85	S19
Set2_ID01.2	Per-emb 12 B	NGC 1333 IRAS 4A2	03:29:10.44	31:13:32.08	6.9	0 $''$ 66×0 $''$ 42	1 $''$ 33×0 $''$ 81	10.04	S19
Set2_ID02	Per-emb 13	NGC 1333 IRAS 4B1	03:29:12.02	31:13:07.99	7.1	0 $''$ 66×0 $''$ 42	1 $''$ 07×0 $''$ 83	14.76	S19
Set2_ID02.2	IRAS4B'	NGC 1333 IRAS 4B2	03:29:12.85	31:13:06.87	7.1	0 $''$ 66×0 $''$ 42	0 $''$ 83×0 $''$ 74	7.13	S19
Set2_ID03	Per-emb 27	NGC 1333 IRAS 2A	03:28:55.57	31:14:36.97	6.5	0 $''$ 66×0 $''$ 42	0 $''$ 93×0 $''$ 66	5.79	Y20
Set2_ID04	Per-emb 54	NGC 1333 IRAS 6	03:29:01.55	31:20:20.49	7.9	0 $''$ 66×0 $''$ 42	0 $''$ 69×0 $''$ 40	0.07	S19
Set2_ID05	Per-emb 21	NGC 1333 IRAS 7 SM2	03:29:10.67	31:18:20.16	8.6	0 $''$ 66×0 $''$ 42	0 $''$ 74×0 $''$ 48	2.05	Y20
Set2_ID06	Per-emb 14	NGC 1333 IRAS 4C	03:29:13.55	31:13:58.12	7.9	0 $''$ 66×0 $''$ 42	0 $''$ 79×0 $''$ 50	3.05	S19
Set2_ID07	Per-emb 35 A	NGC 1333 IRAS 1	03:28:37.10	31:13:30.77	7.4	0 $''$ 66×0 $''$ 42	0 $''$ 75×0 $''$ 51	0.93	Y20
Set2_ID07.2	Per-emb 35 B	NGC 1333 IRAS 1	03:28:37.22	31:13:31.74	7.3	0 $''$ 66×0 $''$ 42	0 $''$ 78×0 $''$ 53	0.75	Y20
Set2_ID08	SVS 13B	NGC 1333 SVS 13B	03:29:03.08	31:15:51.73	8.5	0 $''$ 66×0 $''$ 42	0 $''$ 87×0 $''$ 68	6.64	S19
Set2_ID09	Per-emb 15		03:29:04.06	31:14:46.23	6.8	0 $''$ 66×0 $''$ 42	0 $''$ 89×0 $''$ 70	0.17	S19
Set2_ID11	Per-emb 50	IRAS 03260+3111 A	03:29:07.77	31:21:57.11	9.3	0 $''$ 66×0 $''$ 42	0 $''$ 73×0 $''$ 44	4.13	Y20
Set2_ID12	Per-emb 18	NGC 1333 IRAS 7 SM1	03:29:11.27	31:18:31.09	8.1	0 $''$ 66×0 $''$ 42	0 $''$ 84×0 $''$ 73	3.42	S19
Set2_ID13	Per-emb 37		03:29:18.97	31:23:14.28	7.5	0 $''$ 67×0 $''$ 42	0 $''$ 82×0 $''$ 57	0.56	Y20
Set2_ID13.2	EDJ2009-235		03:29:18.26	31:23:19.73	7.7	0 $''$ 67×0 $''$ 42	0 $''$ 66×0 $''$ 44	0.26	Y20
Set2_ID13.3	EDJ2009-237		03:29:18.74	31:23:25.24	...	0 $''$ 67×0 $''$ 42	0 $''$ 67×0 $''$ 42	0.12	...
Set2_ID14	Per-emb 60		03:29:20.05	31:24:07.35	...	0 $''$ 67×0 $''$ 42	0 $''$ 73×0 $''$ 47	0.08	...
Set2_ID15	EDJ2009-172		03:28:56.65	31:18:35.43	...	0 $''$ 66×0 $''$ 42	0 $''$ 69×0 $''$ 44	0.62	...
Set2_ID16	Per-emb 36	NGC 1333 IRAS 2B	03:28:57.37	31:14:15.77	6.9	0 $''$ 66×0 $''$ 42	0 $''$ 73×0 $''$ 46	5.56	S19
Set3_ID00	B1-b S		03:33:21.36	31:07:26.34	6.6	0 $''$ 46×0 $''$ 30	0 $''$ 63×0 $''$ 53	14.79	C16
Set3_ID00.2	B1-b N		03:33:21.21	31:07:43.63	6.6	0 $''$ 46×0 $''$ 30	0 $''$ 56×0 $''$ 47	7.67	C16
Set3_ID01	Per-emb 29	B1-c	03:33:17.88	31:09:31.74	6.1	0 $''$ 46×0 $''$ 30	0 $''$ 56×0 $''$ 39	8.41	Y20
Set3_ID02	Per-emb 10	B1-d	03:33:16.43	31:06:52.01	6.4	0 $''$ 46×0 $''$ 30	0 $''$ 49×0 $''$ 32	1.82	S19
Set3_ID03	Per-emb 40	B1-a	03:33:16.67	31:07:54.87	7.4	0 $''$ 46×0 $''$ 30	0 $''$ 47×0 $''$ 32	1.44	S19
Set3_ID04	Per-emb 2	IRAS 03292+3039	03:32:17.92	30:49:47.81	7.0	0 $''$ 45×0 $''$ 30	1 $''$ 35×0 $''$ 97	7.41	S19
Set3_ID05	Per-emb 5	IRAS 03282+3035	03:31:20.94	30:45:30.24	7.3	0 $''$ 45×0 $''$ 30	0 $''$ 56×0 $''$ 41	15.29	S19
Set3_ID06	Per-emb 1	HH 211 MMS	03:43:56.81	32:00:50.16	9.4	0 $''$ 49×0 $''$ 32	0 $''$ 68×0 $''$ 48	4.57	S19
Set3_ID07	Per-emb 11 A	IC 348 MMS	03:43:57.07	32:03:04.76	9.0	0 $''$ 50×0 $''$ 33	0 $''$ 61×0 $''$ 48	10.47	S19
Set3_ID07.2	Per-emb 11 B	IC 348 MMS	03:43:56.88	32:03:03.08	9.0	0 $''$ 50×0 $''$ 33	0 $''$ 92×0 $''$ 69	0.40	S19
Set3_ID07.3	Per-emb 11 C	IC 348 MMS	03:43:57.70	32:03:09.82	9.0	0 $''$ 50×0 $''$ 33	1 $''$ 10×0 $''$ 86	0.34	S19
Set3_ID08	Per-emb 8		03:44:43.98	32:01:35.19	11.0	0 $''$ 50×0 $''$ 32	0 $''$ 49×0 $''$ 36	8.51	S19
Set3_ID08.2	Per-emb 55	IRAS 03415+3152	03:44:43.30	32:01:31.22	12.0	0 $''$ 50×0 $''$ 32	0 $''$ 49×0 $''$ 33	0.32	S19
Set3_ID09	Per-emb 16		03:43:50.97	32:03:24.12	8.8	0 $''$ 50×0 $''$ 32	0 $''$ 61×0 $''$ 52	0.35	S19
Set3_ID09.2	Per-emb 28		03:43:51.01	32:03:08.02	8.6	0 $''$ 50×0 $''$ 32	0 $''$ 56×0 $''$ 32	1.52	S19
Set3_ID10	Per-emb 53	B5 IRS 1	03:47:41.59	32:51:43.62	10.2	0 $''$ 51×0 $''$ 33	0 $''$ 58×0 $''$ 42	1.55	Y20

**References**—C16=Carney et al. (2016); H18=Higuchi et al. (2018); S18=Stephens et al. (2018); S19=Stephens et al. (2019); Y20=this study.

mask to the entire primary beam as a continuum source is detected toward the edge of the primary beam where the noise is elevated.

- Extracting spectra: We use the CASA task `specflux` to extract the mean flux density within the ellipse which has the same major and minor axes as well as the position angle as the fitted continuum sources.
- Baseline calibration: The continuum has been removed before the imaging process; however, the extracted spectra sometimes still show imperfect baselines. The spectra show significant differences from one to another such as rich emission lines, lack of emission, and broad emission features. Thus, we manually select the frequency ranges for baseline calibration for each spectral window and each field.
- Velocity correction: Finally, the frequency of the extracted spectra are corrected according to the source velocities. We collect the source velocities from the literature as well as from the strong emission lines in our spectra. Table 1 lists the adopted source velocities and the corresponding references.

Figure 1 shows the images of the continuum along with the fitted shapes, while the properties of the continuum sources are listed in Table 1. Our observations detect 50 continuum sources. The continuum emission appears as compact circular or elliptical shape with no sub-structure. Some sources show extended continuum emission resembling the shape of outflow cavities.

Three sources, EDJ2009-237, Per-emb-60, and EDJ2009-172, have no spectral line detected; therefore, we exclude them from spectral extraction as well as the line identification and modeling. These three sources still need to be included for detection number statistics.

### 3.1. Line Identifications and Modeling

Line identification starts with manual identification and verification for a few sources with rich spectra, including Per-emb-12B and B1-bS. We use SPLATALOGUE<sup>1</sup> to identify the molecular species and use XCLASS (Möller et al. 2017) to verify the identification. The XCLASS package is a LTE radiative transfer code that uses the molecular data from the Cologne Database of Molecular Spectroscopy (CDMS; Müller et al. 2001, 2005; Endres et al. 2016) and the Jet Propulsion Laboratory (JPL; Pickett et al. 1998). An identification needs to satisfy the following criteria.

- The spectra agree with the predicted strengths of the model.
- The spectral lines are not all blended with other emission, such as other molecules and the SiO emission tracing the outflows. The emission of a few species, such as HDCO & <sup>13</sup>CH<sub>3</sub>OH, CH<sub>3</sub>CHO & CH<sub>2</sub>DOH, <sup>34</sup>SO & C<sub>2</sub>H<sub>5</sub>OH, and CH<sub>3</sub>OCH<sub>3</sub> & CH<sub>2</sub>DCN, are partially blended (blending occurs at a few lines but other lines remain isolated). The fittings of those species are performed together to verify their identification.
- Identified molecules need to be already found toward young stellar objects as summarized in McGuire (2018).

Table 3 lists the identified species and transitions. Only identifiable transitions are listed. The XCLASS modeling includes all the transitions in our frequency coverage regardless their Einstein-A values and upper energy levels.

Systematic spectral fitting using XCLASS is then applied to all sources using a list of species, compiled from the identifications. Appendix A lists The catalogs used in this study. The fitting function in XCLASS includes several optimization algorithms that can be used in series to reduce biases. We configure the algorithm chain that starts with the genetic algorithm followed by the Levenberg-Marquardt  $\chi^2$  minimization. The genetic algorithm searches the best-fitting parameters iteratively with generations that evolve like a natural selection, where the better fitting models get less modification over generations. We setup the genetic algorithm to search for the top two best-fitting models with 30 generations. Then, the Levenberg-Marquardt  $\chi^2$  minimization applies to the two best-fitting models for 20 iterations to find the best-fitting models. The genetic algorithm aims to find local minimums and the Levenberg-Marquardt minimization further finds the best-fitting models in the local minimums. The two best-fitting models found by the genetic algorithm often very similar, suggesting that there is only one minimum. To address the rare cases of two separated local minimums, we pick the model with the lower  $\chi^2$  values from the two best-fitting models constrained by the Levenberg-Marquardt minimization.

There are four parameters for the XCLASS modeling, the size of the emitting molecule ( $r_{\text{COM}}$ ), the excitation temperature ( $T_{\text{ex}}$ ), the column density ( $N_{\text{COM}}$ ), and the line width ( $\Delta\nu$ ). We assume the COMs are all concentrated at the center, simplified as a 2D thin circular disk. We fix  $r_{\text{COM}}$  as 0''.5, similar to our beam size, and optimize the model with five excitation temperatures, 100, 150, 200, 250, and 300 K. We allow the line width varying between 1.2 km s<sup>-1</sup> to 3.5 km s<sup>-1</sup> for better fitting

<sup>1</sup> <http://www.splatalogue.net/>



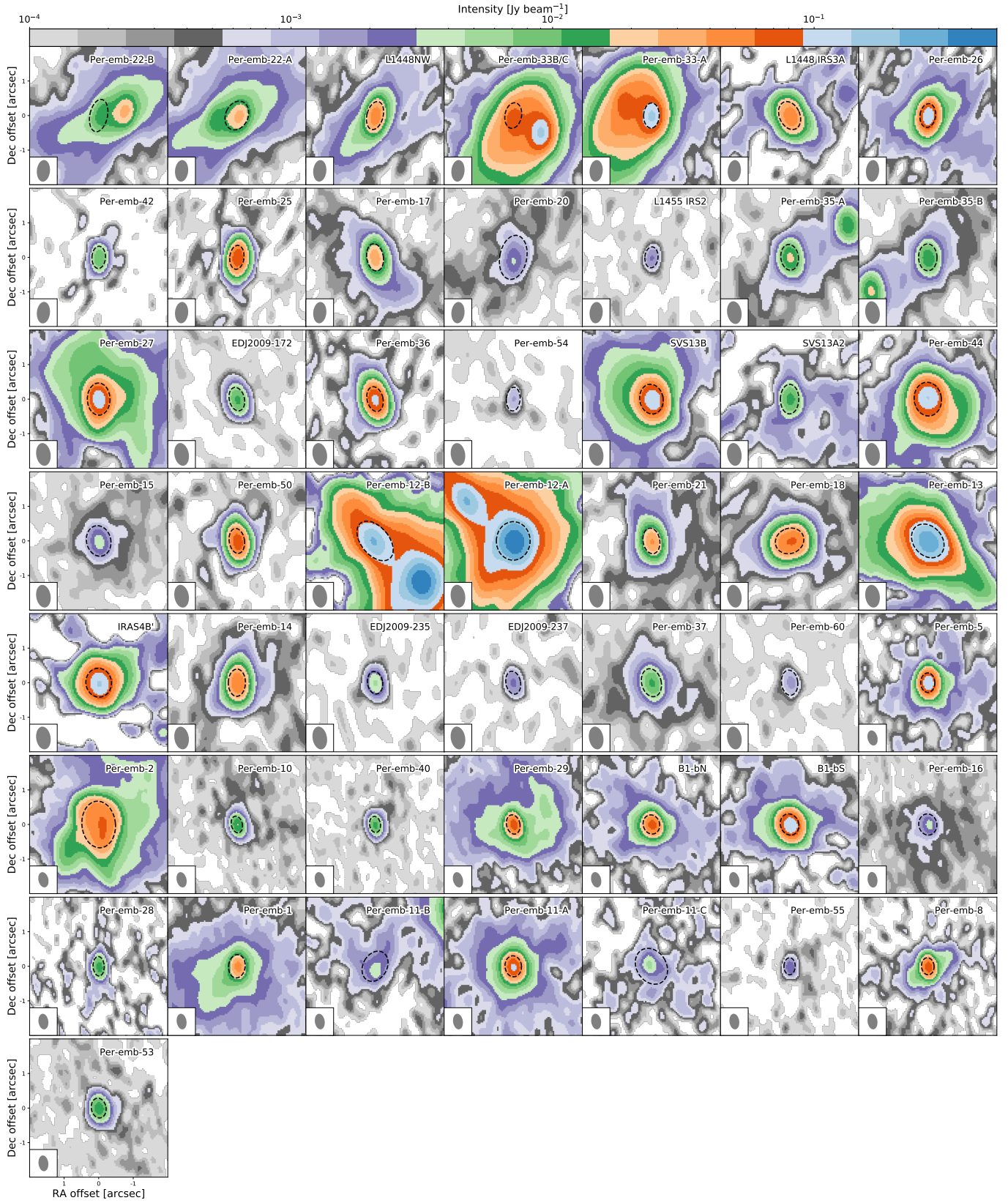


**Figure 1.** The continuum images of all PEACHES protostars. Non-detections toward L1448 IRS 2E and NGC 1333 SVS 3 are not shown. The dashed ellipses illustrate the size of fitted continuum, which is the region for extracting 1D spectra.

quality, and the allowed range of the column density for each molecule is chosen according to the strength of the emission. If a molecule is detected, the mean column densities will be the best-fitting column density, while the range of the column densities indicates the upper

and lower uncertainty. If a molecule is non-detection, the synthetic spectra for all lines are scaled to match the peaks of the each line fitted by a Gaussian profile. Then, we take the minimum of the corresponding column densities as the upper limit.

**Table 3.** Line Identification

Frequency (MHz)	Transition <sup>a</sup>	log(Einstein-A)	$E_u$ (K)	$g_u$	Ref.
Ethyne (CCH)					
262065.00 (0.05)	[3, 5/2, 3]→[2, 3/2, 2] <sup>b</sup>	-4.31	25.16	7	CDMS
262067.47 (0.05)	[3, 5/2, 2]→[2, 3/2, 1] <sup>b</sup>	-4.35	25.16	5	CDMS
262078.93 (0.02)	[3, 5/2, 2]→[2, 3/2, 2] <sup>b</sup>	-5.22	25.16	5	CDMS
Cyclopropenylidene (c-C <sub>3</sub> H <sub>2</sub> )					
244222.15 (0.01)	[3, 2, 1]→[2, 1, 2]	-4.23	18.17	21	CDMS
246557.77 (0.02)	[16, 10, 7]→[16, 9, 8]	-3.36	397.83	99	CDMS
260479.75 (0.02)	[5, 3, 2]→[4, 4, 1]	-3.79	44.72	33	CDMS
Methanol (CH <sub>3</sub> OH $v_t = 0$ )					
243915.79 (0.01)	[5, 1, 4]→[4, 1, 3] A	-4.22	49.66	44	CDMS
246074.61 (0.02)	[20, 3, 17]→[20, 2, 18] A	-4.08	537.03	164	CDMS
246873.30 (0.02)	[19, 3, 16]→[19, 2, 17] A	-4.08	490.65	156	CDMS
261805.68 (0.01)	[2, 1, 1]→[1, 0, 1] E	-4.25	28.01	20	CDMS
Methanol ( <sup>13</sup> CH <sub>3</sub> OH $v_t = 0$ )					
246426.12 (0.22)	[23, 4, 19]→[22, 5, 18]	-4.58	721.02	47	CDMS
247086.3 (0.5)	[23, 3, 20]→[23, 2, 21] A→ A+	-4.07	674.86	47	CDMS
259036.49 (0.17)	[17, 3, 15]→[17, 2, 16] A+→ A-	-4.04	396.48	35	CDMS
Methanol (CH <sub>2</sub> DOH $v_t = 0$ )					
243514.31 (0.01)	[9, 2, 8]→[10, 1, 10] o <sub>1</sub>	-5.17	131.85	19	JPL
246973.11 (0.01)	[4, 1, 4]→[4, 1, 3] e <sub>1</sub>	-4.67	37.69	9	JPL
260543.63 (0.01)	[3, 2, 1]→[3, 1, 2] o <sub>1</sub>	-4.65	48.34	7	JPL
Methanol (CH <sub>3</sub> <sup>18</sup> O $v_t = 0$ )					
246256.60 (0.04)	[11, 2, 10]→[10, 3, 7] A	-4.64	184.27	92	CDMS
Sulfur monoxide (SO <sup>3</sup> Σ)					
258255.83 (0.01)	[N, J]=[6, 6]→[5, 5]	-3.67	56.50	13	CDMS
261843.72 (0.03)	[N, J]=[7, 6]→[6, 5]	-3.64	47.55	15	CDMS
Sulfur monoxide ( <sup>34</sup> SO)					
246663.47 (0.1)	[N, J]=[5, 6]→[4, 5]	-3.74	49.89	11	CDMS
Sulfur dioxide (SO <sub>2</sub> )					
244254.22 (0.01)	[14, 0, 14]→[13, 1, 13]	-3.79	93.90	29	CDMS
Hydrogen cyanide (H <sup>13</sup> CN)					
259010.26 (0.01)	[J, F]=[3, 3]→[2, 3]	-4.07	24.86	7	CDMS
259011.55 (0.01)	[J, F]=[3, 2]→[2, 1]	-3.19	24.86	5	CDMS
259011.80 (0.01)	[J, F]=[3, 3]→[2, 2]	-3.16	24.86	7	CDMS
259011.86 (0.01)	[J, F]=[3, 4]→[2, 3]	-3.11	24.86	9	CDMS
259012.34 (0.01)	[J, F]=[3, 2]→[2, 3]	-5.46	24.86	5	CDMS
259013.89 (0.01)	[J, F]=[3, 2]→[2, 2]	-3.92	24.86	5	CDMS
Carbon Monosulfide (CS)					
244935.56 (0.01)	[J]=[5]→[4]	-3.53	35.27	11	CDMS
Formaldehyde (HDCO)					
246924.6 (0.1)	[4, 1, 4]→[3, 1, 3]	-3.40	37.60	9	CDMS
259034.9 (0.1)	[4, 2, 2]→[3, 2, 1]	-3.44	62.86	9	CDMS
Methyl formate (CH <sub>3</sub> OCHO)					
245883.2 (0.1)	[20, 13, 7]→[19, 13, 6] E	-3.89	235.98	82	JPL
245885.2 (0.1)	[20, 13, 7]→[19, 13, 6] A	-3.89	235.98	82	JPL

Table 3 continued

Table 3 (continued)

Frequency (MHz)	Transition <sup>a</sup>	log(Einstein-A)	$E_u$ (K)	$g_u$	Ref.
245885.2 (0.1)	[20, 13, 8]→[19, 13, 7] A	−3.89	235.98	82	JPL
245903.7 (0.1)	[20, 13, 8]→[19, 13, 7] E	−3.89	235.97	82	JPL
246027.5 (0.1)	[21, 2, 19]→[20, 3, 18] E	−4.63	139.85	86	JPL
246038.9 (0.1)	[21, 2, 19]→[20, 3, 18] A	−4.63	139.85	86	JPL
246054.8 (0.1)	[20, 12, 8]→[19, 12, 7] E	−3.84	219.43	82	JPL
246060.8 (0.1)	[20, 12, 8/9]→[19, 12, 7/8] A	−3.84	219.43	82	JPL
246076.9 (0.1)	[20, 12, 9]→[19, 12, 8] E	−3.84	219.41	82	JPL
246285.4 (0.1)	[20, 11, 9]→[19, 11, 8] E	−3.80	204.21	82	JPL
246295.1 (0.1)	[20, 11, 10]→[19, 11, 9] A	−3.80	204.21	82	JPL
246295.1 (0.1)	[20, 11, 9]→[19, 11, 8] A	−3.80	204.21	82	JPL
246308.3 (0.1)	[20, 11, 10]→[19, 11, 9] E	−3.80	204.20	82	JPL
246456.1 (0.1)	[10, 5, 6]→[9, 4, 5] E	−5.52	49.09	42	JPL
246600.0 (0.1)	[20, 10, 10]→[19, 10, 9] E	−3.77	190.34	82	JPL
246613.4 (0.1)	[20, 10, 11]→[19, 10, 10] A	−3.77	190.34	82	JPL
246613.4 (0.1)	[20, 10, 10]→[19, 10, 9] A	−3.77	190.34	82	JPL
246623.2 (0.1)	[20, 10, 11]→[19, 10, 10] E	−3.77	190.34	82	JPL
246660.5 (0.1)	[10, 5, 6]→[9, 4, 5] A	−4.74	49.08	42	JPL
246675.4 (0.1)	[15, 4, 12]→[14, 3, 11] E	−4.93	81.85	62	JPL
246683.5 (0.1)	[15, 4, 12]→[14, 3, 11] A	−4.93	81.84	62	JPL
246752.9 (0.1)	[10, 5, 5]→[9, 4, 5] E	−4.90	49.10	42	JPL
246891.6 (0.1)	[19, 4, 15]→[18, 4, 14] E	−3.66	126.22	78	JPL
246914.7 (0.1)	[19, 4, 15]→[18, 4, 14] A	−3.66	126.22	78	JPL
246945.7 (0.1)	[10, 5, 6]→[9, 4, 6] E	−4.90	49.09	42	JPL
247040.7 (0.1)	[20, 9, 11]→[19, 9, 10] E	−3.74	177.83	82	JPL
247044.1 (0.1)	[21, 3, 19]→[20, 3, 18] E	−3.66	139.90	86	JPL
247053.5 (0.1)	[21, 3, 19]→[20, 3, 18] A	−3.66	139.89	86	JPL
247057.3 (0.1)	[20, 9, 12]→[19, 9, 11] A	−3.74	177.83	82	JPL
247057.7 (0.1)	[20, 9, 11]→[19, 9, 10] A	−3.74	177.83	82	JPL
247063.7 (0.1)	[20, 9, 12]→[19, 9, 11] E	−3.74	177.83	82	JPL
247124.3 (0.1)	[10, 5, 5]→[9, 4, 6] E	−4.74	49.08	42	JPL
258275.0 (0.1)	[21, 13, 8]→[20, 13, 7] E	−3.79	248.37	86	JPL
258277.4 (0.1)	[21, 13, 8]→[20, 13, 7] A	−3.79	248.37	86	JPL
258277.4 (0.1)	[21, 13, 9]→[20, 13, 8] A	−3.79	248.37	86	JPL
259341.9 (0.1)	[24, 0, 24]→[23, 1, 23] E	−4.37	158.23	98	JPL
259342.0 (0.1)	[24, 1, 24]→[23, 1, 23] E	−3.58	158.23	98	JPL
259342.1 (0.1)	[24, 0, 24]→[23, 0, 23] E	−3.58	158.23	98	JPL
259342.3 (0.1)	[24, 1, 24]→[23, 0, 23] E	−4.37	158.23	98	JPL
259342.7 (0.1)	[24, 0, 24]→[23, 1, 23] A	−4.37	158.22	98	JPL
259342.9 (0.1)	[24, 1, 24]→[23, 1, 23] A	−3.58	158.22	98	JPL
259343.0 (0.1)	[24, 0, 24]→[23, 0, 23] A	−3.58	158.22	98	JPL
259343.2 (0.1)	[24, 1, 24]→[23, 0, 23] A	−4.37	158.22	98	JPL
261822.3 (0.1)	[17, 10, 7]→[17, 9, 8] A	−4.73	156.63	70	JPL
262088.2 (0.1)	[16, 10, 6]→[16, 9, 7] A	−4.76	146.59	66	JPL
262088.2 (0.1)	[16, 10, 7]→[16, 9, 8] A	−4.76	146.59	66	JPL
Methyl formate (CH <sub>3</sub> OCHO $v = 1$ )					
243511.5 (0.1)	[20, 12, 8]→[19, 12, 7] E	−3.85	407.25	82	JPL
245846.9 (0.1)	[21, 3, 19]→[20, 3, 18] E	−3.66	326.30	86	JPL
246106.8 (0.1)	[20, 7, 14]→[19, 7, 13] A	−3.70	343.77	82	JPL
246184.2 (0.1)	[20, 8, 13]→[19, 8, 12] E	−3.72	353.27	82	JPL
246187.0 (0.1)	[21, 2, 19]→[20, 2, 18] A	−3.66	326.62	86	JPL
246233.6 (0.1)	[20, 7, 13]→[19, 7, 12] A	−3.70	343.79	82	JPL
246274.9 (0.1)	[20, 7, 13]→[19, 7, 12] E	−3.70	343.86	82	JPL
246410.95 (0.01)	[10, 5, 5]→[9, 4, 6] A	−4.73	236.70	42	JPL
246422.7 (0.1)	[22, 1, 21]→[21, 2, 20] A	−4.51	330.43	90	JPL

Table 3 continued

**Table 3** (*continued*)

Frequency (MHz)	Transition <sup>a</sup>	log(Einstein-A)	$E_u$ (K)	$g_u$	Ref.
246461.2 (0.1)	[22, 2, 21]→[21, 2, 20] A	−3.65	330.43	90	JPL
246488.4 (0.1)	[22, 1, 21]→[21, 1, 20] A	−3.65	330.43	90	JPL
246562.9 (0.1)	[21, 2, 19]→[20, 2, 18] E	−3.66	326.24	86	JPL
246706.5 (0.1)	[22, 2, 21]→[21, 2, 20] E	−3.65	329.89	90	JPL
246731.7 (0.1)	[22, 1, 21]→[21, 1, 20] E	−3.65	329.89	90	JPL
246985.2 (0.1)	[20, 6, 15]→[19, 6, 14] A	−3.68	335.37	82	JPL
259003.9 (0.1)	[21, 7, 14]→[20, 7, 13] A	−3.63	356.22	86	JPL
259025.8 (0.1)	[21, 7, 14]→[20, 7, 13] E	−3.63	356.29	86	JPL
260479.6 (0.1)	[44, 9, 36]→[44, 8, 37] A	−4.59	828.74	178	JPL
Dimethyl ether (CH <sub>3</sub> OCH <sub>3</sub> )					
246499.29 (0.01)	[37, 6, 31]→[37, 5, 12] AA	−4.01	693.72	750	CDMS
246505.09 (0.01)	[37, 6, 31]→[37, 5, 12] AE	−4.01	693.72	450	CDMS
246505.09 (0.01)	[37, 6, 31]→[37, 5, 12] EA	−4.01	693.72	300	CDMS
246697.43 (0.01)	[27, 4, 23]→[26, 5, 21] AA	−4.70	367.61	330	CDMS
246697.87 (0.01)	[27, 4, 23]→[26, 5, 21] EE	−4.70	367.61	880	CDMS
246698.31 (0.01)	[27, 4, 23]→[26, 5, 21] AE	−4.70	367.61	110	CDMS
246698.31 (0.01)	[27, 4, 23]→[26, 5, 21] EA	−4.70	367.61	220	CDMS
259305.22 (0.01)	[33, 3, 31]→[34, 6, 28] AA	−6.61	563.02	670	CDMS
259308.39 (0.01)	[33, 3, 31]→[34, 6, 28] AE	−6.61	563.02	402	CDMS
259308.39 (0.01)	[33, 3, 31]→[34, 6, 28] EA	−6.61	563.02	268	CDMS
259309.47 (0.01)	[17, 5, 12]→[17, 4, 13] AE	−4.06	174.54	210	CDMS
259309.76 (0.01)	[17, 5, 12]→[17, 4, 13] EA	−4.06	174.54	140	CDMS
259311.95 (0.01)	[17, 5, 12]→[17, 4, 13] EE	−4.06	174.54	560	CDMS
259314.28 (0.01)	[17, 5, 12]→[17, 4, 13] AA	−4.06	174.54	350	CDMS
Acetone (CH <sub>3</sub> COCH <sub>3</sub> )					
244218.91 (0.01)	[20, 5, 15]→[19, 6, 14] AE	−3.32	139.69	82	JPL
244218.91 (0.01)	[20, 6, 15]→[19, 5, 14] AE	−3.32	139.69	250	JPL
244218.92 (0.01)	[20, 5, 15]→[19, 6, 14] EA	−3.32	139.69	160	JPL
244218.92 (0.01)	[20, 6, 15]→[19, 5, 14] EA	−3.32	139.69	160	JPL
245831.34 (0.09)	[13, 10, 3]→[12, 9, 4] EE	−3.80	77.84	432	JPL
246400.99 (0.05)	[34, 7, 28]→[34, 5, 29] EE	−4.17	364.98	1100	JPL
246400.99 (0.05)	[34, 6, 28]→[34, 5, 29] EE	−4.03	364.98	1100	JPL
246400.99 (0.05)	[34, 7, 28]→[34, 6, 29] EE	−4.03	364.98	1100	JPL
246400.99 (0.05)	[34, 6, 28]→[34, 6, 29] EE	−4.17	364.98	1100	JPL
246404.27 (0.01)	[22, 3, 19]→[21, 4, 18] AE	−3.23	149.62	90	JPL
246404.27 (0.01)	[22, 4, 19]→[21, 3, 18] AE	−3.23	149.62	270	JPL
246404.29 (0.01)	[22, 3, 19]→[21, 4, 18] EA	−3.23	149.62	180	JPL
246404.29 (0.01)	[22, 4, 19]→[21, 3, 18] EA	−3.23	149.62	180	JPL
246450.40 (0.01)	[22, 4, 19]→[21, 3, 18] EE	−3.23	149.57	720	JPL
246450.40 (0.01)	[22, 3, 19]→[21, 3, 18] EE	−5.09	149.57	720	JPL
246450.40 (0.01)	[22, 3, 19]→[21, 4, 18] EE	−3.24	149.57	720	JPL
246450.40 (0.01)	[22, 4, 19]→[21, 4, 18] EE	−4.92	149.57	720	JPL
246496.17 (0.46)	[25, 14, 12]→[24, 15, 9] AE	−5.01	257.11	100	JPL
246496.47 (0.02)	[22, 3, 19]→[21, 4, 18] AA	−3.23	149.51	270	JPL
246496.47 (0.02)	[22, 4, 19]→[21, 3, 18] AA	−3.23	149.51	450	JPL
246714.12 (0.05)	[9, 8, 1]→[8, 5, 4] EA	−5.84	40.59	76	JPL
246714.94 (0.05)	[32, 4, 28]→[32, 4, 29] EA	−3.97	305.61	260	JPL
246714.94 (0.05)	[32, 5, 28]→[32, 3, 29] EA	−3.97	305.61	260	JPL
246715.04 (0.05)	[32, 5, 28]→[32, 4, 29] AE	−3.97	305.61	390	JPL
246715.04 (0.05)	[32, 4, 28]→[32, 3, 29] EA	−3.97	305.61	130	JPL
246719.92 (0.04)	[33, 6, 28]→[33, 4, 29] EE	−5.62	344.85	1100	JPL
246719.92 (0.04)	[33, 5, 28]→[33, 4, 29] EE	−3.87	344.85	1100	JPL
246719.92 (0.04)	[33, 6, 28]→[33, 5, 29] EE	−3.87	344.85	1100	JPL
246719.92 (0.04)	[33, 5, 28]→[33, 5, 29] EE	−5.61	344.85	1100	JPL

*Table 3 continued*



**Table 3** (*continued*)

Frequency (MHz)	Transition <sup>a</sup>	log(Einstein-A)	$E_u$ (K)	$g_u$	Ref.
261818.11 (0.01)	[20, 7, 13]→[19, 8, 12] EA	−3.31	151.17	160	JPL
261818.17 (0.01)	[20, 7, 13]→[19, 8, 12] AE	−3.31	151.17	82	JPL
261819.09 (0.01)	[20, 8, 13]→[19, 7, 12] EA	−3.31	151.17	160	JPL
261819.17 (0.01)	[20, 8, 13]→[19, 7, 12] AE	−3.31	151.17	250	JPL
Methyl cyanide (CH <sub>3</sub> CN)					
257507.56 (0.01)	[ $N$ , $K$ ]=[14, 2]→[13, 2]	−3.00	121.28	58	JPL
257522.43 (0.01)	[ $N$ , $K$ ]=[14, 1]→[13, 1]	−2.99	99.84	58	JPL
257527.38 (0.01)	[ $N$ , $K$ ]=[14, 0]→[13, 0]	−2.99	92.70	58	JPL
Acetaldehyde (CH <sub>3</sub> CHO $v_t = 0$ )					
246330.73 (0.01)	[15, 3, 13]→[15, 2, 14] A	−4.29	131.49	62	JPL
260530.40 (0.01)	[14, 1, 14]→[13, 1, 13] E	−3.20	96.39	58	JPL
260544.02 (0.01)	[14, 1, 14]→[13, 1, 13] A	−3.20	96.32	58	JPL
260547.46 (2.07)	[9, 4, 5]→[9, 3, 7] E, $v_t = 2$	−6.06	456.38	38	JPL
gauche-Ethanol ( $g$ -C <sub>2</sub> H <sub>5</sub> OH)					
246414.76 (0.05)	[14, 3, 11]→[13, 3, 10] $v_t = 0 \rightarrow 0$	−3.89	155.72	29	JPL
246524.28 (0.01)	[13, 2, 12]→[12, 1, 12] $v_t = 0 \rightarrow 1$	−4.50	136.95	27	JPL
246658.18 (0.01)	[32, 5, 28]→[32, 4, 29] $v_t = 0 \rightarrow 0$	−6.33	527.94	65	JPL
246662.98 (0.01)	[4, 2, 3]→[3, 1, 3] $v_t = 1 \rightarrow 0$	−4.36	74.77	9	JPL
259322.64 (0.01)	[14, 3, 11]→[13, 2, 11] $v_t = 0 \rightarrow 1$	−4.39	155.72	29	JPL
260457.73 (0.01)	[15, 4, 12]→[14, 4, 11] $v_t = 1 \rightarrow 1$	−3.83	181.10	31	JPL
trans-Ethanol (C <sub>2</sub> H <sub>5</sub> OH)					
246663.62 (0.05)	[24, 1, 23]→[24, 0, 24]	−3.73	252.35	49	JPL
261815.99 (0.05)	[28, 3, 26]→[28, 2, 27]	−3.96	350.98	57	JPL
Glycolaldehyde ( <i>cis</i> -CH <sub>2</sub> OHCHO)					
246773.09 (0.02)	[30, 2, 28]→[30, 1, 29]	−4.04	252.68	61	CDMS
246778.28 (0.02)	[30, 3, 28]→[30, 2, 29]	−4.04	252.68	61	CDMS
262056.78 (0.01)	[25, 2, 24]→[24, 1, 23]	−3.34	158.25	51	CDMS
261795.48 (0.01)	[25, 11, 14]→[25, 10, 15]	−3.57	254.23	51	CDMS
261798.96 (0.01)	[25, 11, 15]→[25, 10, 16]	−3.57	254.23	51	CDMS
Methyl cyanide (CH <sub>2</sub> DCN)					
259315.51 (0.01)	[15, 1, 15]→[14, 1, 14]	−2.82	104.97	31	CDMS
260523.05 (0.01)	[15, 2, 13]→[14, 2, 12]	−2.82	121.60	31	CDMS
Ethyl cyanide (CH <sub>3</sub> CH <sub>2</sub> CN)					
246268.74 (0.01)	[27, 2, 25]→[26, 2, 24]	−2.90	169.80	55	CDMS
246421.92 (0.01)	[28, 2, 27]→[27, 2, 26]	−2.90	177.26	57	CDMS
246548.70 (0.01)	[27, 3, 24]→[26, 3, 23]	−2.90	174.06	55	CDMS
260535.69 (0.05)	[29, 5, 25]→[28, 5, 24]	−2.84	215.06	59	CDMS
Formamide (NH <sub>2</sub> CHO)					
243521.04 (0.01)	[12, 1, 12]→[11, 1, 11]	−2.98	79.19	25	CDMS
Formic acid ( <i>t</i> -HCOOH)					
262103.48 (0.01)	[12, 0, 12]→[11, 0, 11]	−3.69	82.77	25	CDMS

<sup>a</sup> The typical quantum numbers are listed as [ $J$ ,  $K_a$ ,  $K_c$ ] unless specified.

<sup>b</sup> The quantum numbers are [ $N$ ,  $J$ ,  $F$ ]

#### 4. CONTINUUM OPACITY

#### 5. DETECTION STATISTICS

We summarize the fraction of sources with detections of molecules in Figure 2. The detection statistics include COMs, carbon-chain molecules, and the simple organic molecules, such as CS, H<sup>13</sup>CN, SO, <sup>34</sup>SO, and SO<sub>2</sub>. The PEACHES protostars show a great chemical diversity

from no molecule detected (B1-bN) to rich spectra of COMs (e.g. Per-emb-12B). Detections of COMs and the number of COMs detected show no obvious correlation with the bolometric luminosity and bolometric temperature of the protostars, which are conventional evolutionary indicators. Low luminosity sources have fewer COMs detected; however, if COMs mostly come from thermally desorption, the region with  $T > T_{\text{desorption}}$  may be smaller for the low luminosity sources, making

the emission of COMs fainter and reducing our sensitivity to detect COMs. We also compare the detection statistics with the mass derived from 9 mm observations that resolved the sources as a proxy of the central mass (Tychoniec et al. 2018). The detection statistics show no clear correlation with the central mass; however, the sources with smaller central mass have fewer detections of COMs, which may due to their low luminosity.

Several sources have their SiO emission with a broad line width, significantly contaminating the emission of  $\text{CH}_3\text{CH}_2\text{CN}$  and  $\text{CH}_3\text{CHO}$ . In the later quantitative discussion, we exclude the spectral windows contaminated by the SiO emission. For assigning the detections, we can distinguish the emission of  $\text{CH}_3\text{CH}_2\text{CN}$  and  $\text{CH}_3\text{CHO}$  from the broad emission in a few sources, such as  $\text{CH}_3\text{CHO}$  in Per-emb 26.

## 6. CORRELATIONS OF COMS

The chemical evolution of protostars may leave certain patterns in the abundance of molecules as the dynamical evolution determines the density and temperature structures, regulating chemical reactions. Thus, the abundance of COMs and their correlations provide critical information to constrain the chemical evolution at embedded protostars. The fitted column density of COMs indicates the abundance of COMs around protostars. Typically COMs are locked into the ices on dust grains at outer envelope. Therefore, we take the column density of COMs as a proxy of the abundance of COMs.

As described in Section 3.1, we fit the column density and line width with different excitation temperatures, resulting in a range of column density as its uncertainty. The comparison between CCH and  $\text{CH}_3\text{OH}$  shows no correlation between these two molecules (Figure 3), similar to the conclusion in Higuchi et al. (2018). The single dish survey by Graninger et al. (2016) shows a correlation between  $\text{C}_4\text{H}$ , a more complex carbon-chain molecules, and  $\text{CH}_3\text{OH}$ . Outflow activity can promote the formation of CCH, which is more efficiency at warm temperature. In face, the morphology of CCH often traces the outflow cavities seen from CS. Therefore, the lack of correlation between CCH and  $\text{CH}_3\text{OH}$  may be affected by outflows.

Figure 5 shows the correlations of several COMs selected from their detection rates. The column density of  $\text{CH}_3\text{OH}$  best correlates with that of  $\text{CH}_3\text{CN}$ . Belloche et al. (2020) also found the tight correlation between these two molecules from the CALYPSO survey, which has a selective sample. The column densities of  $\text{CH}_3\text{OCH}_3$  and  $\text{CH}_3\text{OCHO}$  also show a tight correlation. To quantify the goodness of correlation, we calculate the Pearson's correlation coefficient ( $r$ ), which tests the lin-

earity of two variables. A simple calculation of the Pearson's correlation coefficient would ignore the uncertainties of the column density. Thus, we use the bootstrapping method to sample the fitted column densities to calculate Pearson's  $r$ , by assuming a normal distribution centers on the best-fitted values with the uncertainty as the width of the normal distribution. If we include the upper limits as normal distributions center on zero, the correlation coefficient becomes significantly lower due to the cluster of samples around zero column density (Figure 4). With the detection-only sample, the mean Pearson's  $r_d$  is 0.91, as expected for a tight correlation, with a Gaussian-like distribution skewed toward lower values. After including the upper limits, the mean Pearson's  $r$  decreases to 0.59 with larger uncertainty (the 68% credible interval increases by 160%). Thus, the bootstrapped correlation coefficient only considers the detected

### 6.1. Excitation Temperatures

#### 6.1.1. $\text{CH}_3\text{OH}$

The PEACHES spectra cover four methanol lines, while the spectra of each source include three of them due to the frequency shift in the wide spectral window. The three methanol lines have upper energy ranging from  $\sim 50$  K to  $\sim 500$  K, which allows us to estimate the rotational temperature of methanol if all three lines are detected. To construct the methanol rotational diagram, we fit the methanol emission with a Gaussian profile and bootstrap the measurements for fitting the rotational temperature. Figure 7 shows the rotational diagram of Per-emb 22 B along with the sampled rotational temperature. The derived rotational temperature of methanol ranges from 120 K to 240 K with an exception of Per-emb 18, which has a rotational temperature of 395.7 K for methanol (Table 4).

## 7. SPATIAL EXTENT OF COMS

## 8. DISCUSSION

### 8.1. Chemical Diversity in PEACHES

### 8.2. Comparison to the CALYPSO Survey

### 8.3. Complex Chemistry throughout Star Formation

### 8.4. 1D Spectra

Y.-L. Yang acknowledges the supports the JSPS Postdoctoral Fellowship from Japan Society for the Promotion of Science. This paper makes use of the following ALMA data: ADS/JAO.ALMA#2016.0.00391.S. ALMA is a partnership of ESO (representing its member states), NSF (USA) and NINS (Japan), together with NRC (Canada), MOST and ASIAA (Taiwan), and

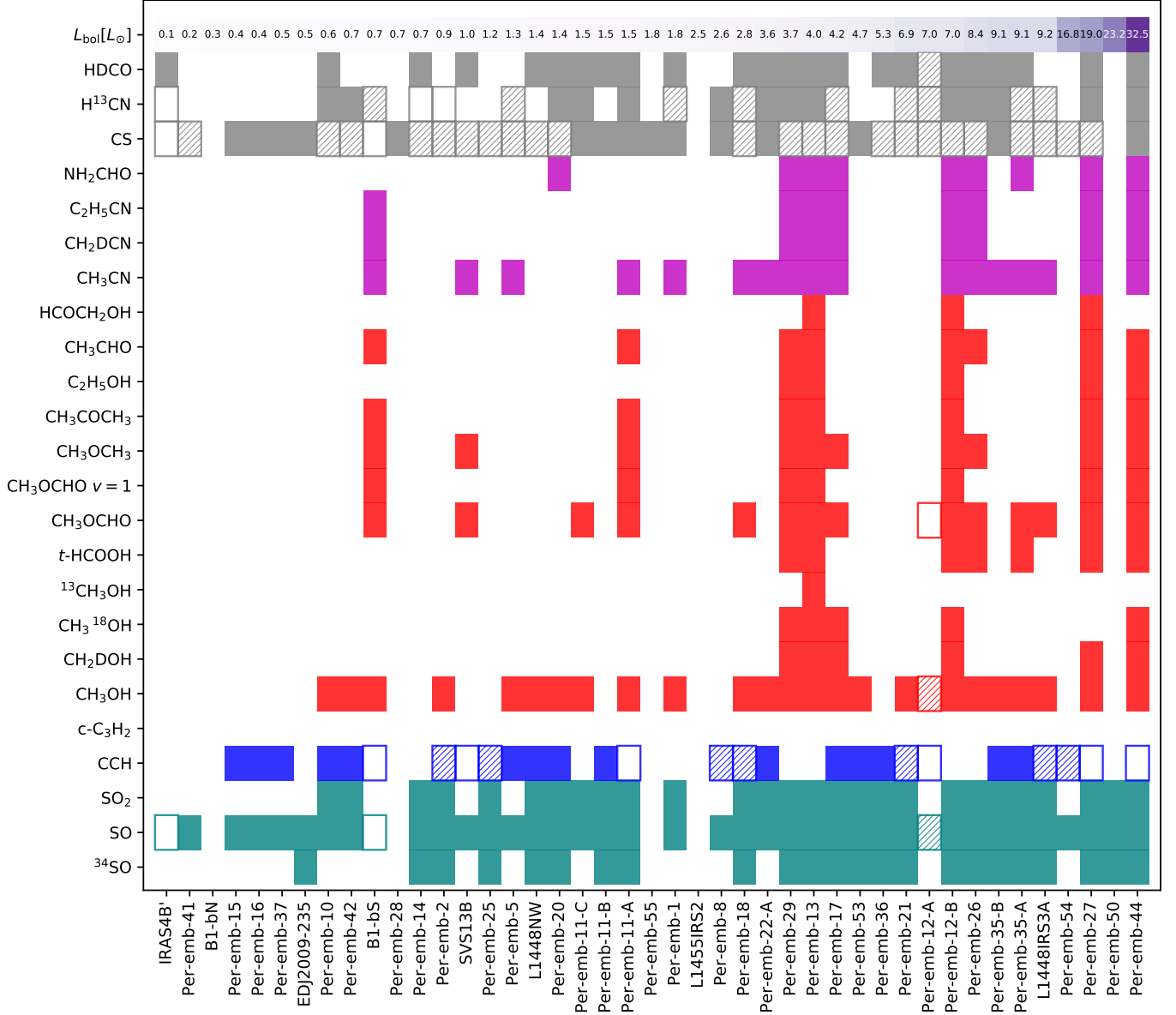


**Figure 2.** The detection statistics sorted by their bolometric luminosity.

KASI (Republic of Korea), in cooperation with the Republic of Chile. The Joint ALMA Observatory is operated by ESO, AUI/NRAO and NAOJ. The National Radio Astronomy Observatory is a facility of the Na-

tional Science Foundation operated under cooperative agreement by Associated Universities, Inc.

*Facilities:* ALMA

*Software:* astropy, XCLASS, spectral-cube, CASA

## APPENDIX

### A. CATALOGS FOR MOLECULAR DATA

#### B. THE SPECTRA OF CCH

The CCH spectra toward the continuum emission have irregular line profiles. Some spectra have strong self-absorption, while some spectra only show the blue-shifted emission. Due to the absorption and irregular line profile, the XCLASS fitting routine often fails to faithfully reproduce the observed CCH spectra. CCH can easily form in the outflow cavity wall due to the abundant  $\text{CH}_4$  sublimated from dust grains as well as  $\text{C}^+$  ionized by the UV radiation.

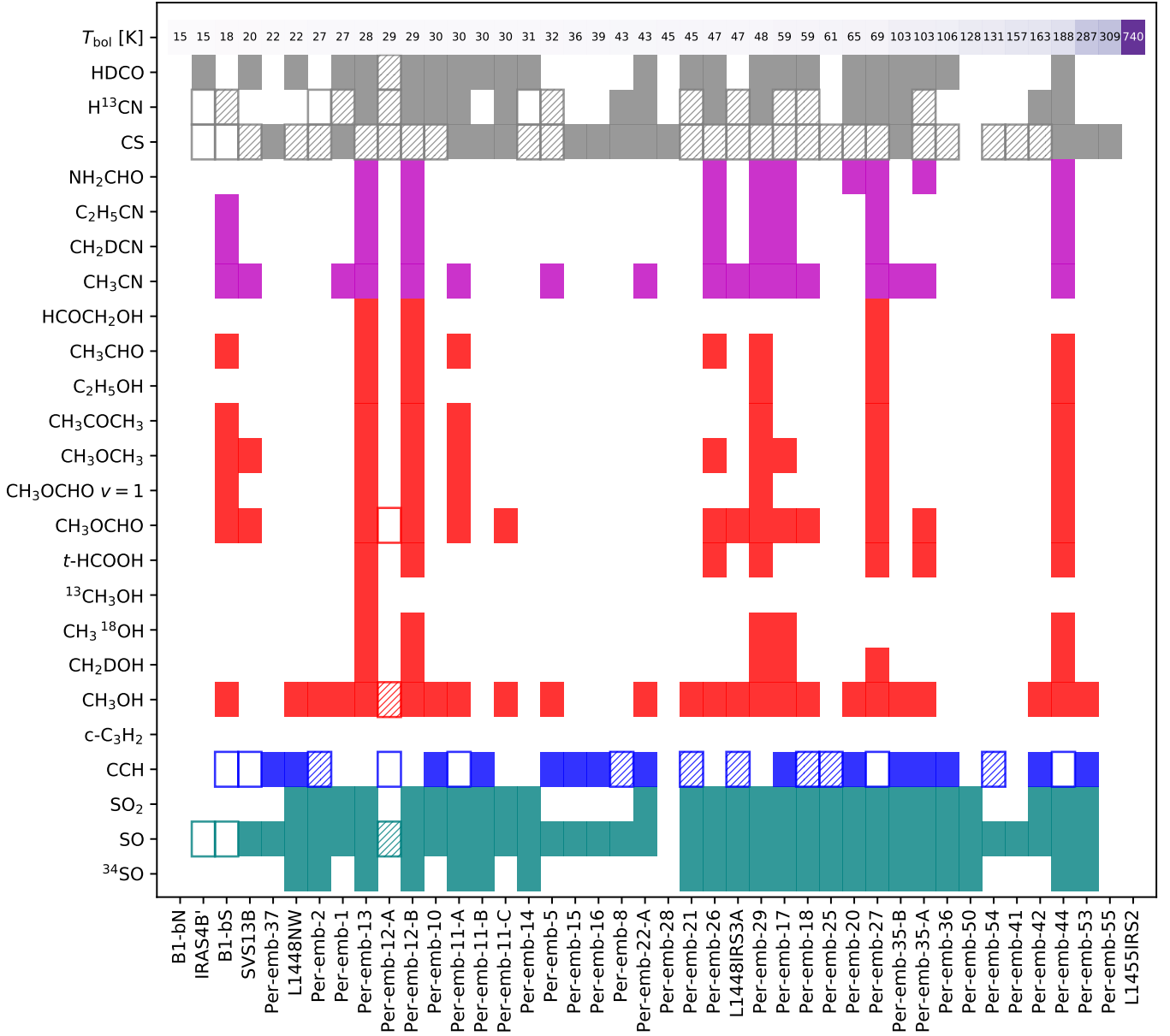


**Figure 2 (Cont.).** The same figure as Figure 2 but sorted by their bolometric temperature.

Thus, the CCH spectra can have broad line width and multiple components. Furthermore, the morphology of the CCH emission traces the outflows, making our extraction from the continuum emission non-ideal for representing the nature of the CCH emission. Figure 11 and Y show the spectra and the moment 0 map of CCH, respectively.

### C. NOTES ON THE 1D SPECTRA

*Per-emb-33-A*—

- The fitting of  $\text{CH}_3\text{OCHO}$  reproduces the the strongest emission at 259343 MHz, but underestimates the emission between 246275 MHz to 247070 MHz, where the emission is at most 0.5 K. Considering the narrow absorption in HCN, CS, and SO lines as well as the brighter continuum temperature (10.5 K), the emission of  $\text{CH}_3\text{OCHO}$  may be affected by the continuum opacity.

*Per-emb-26*—

- Red-shifted excess appears in the  $\text{CH}_3\text{OH}$  lines.

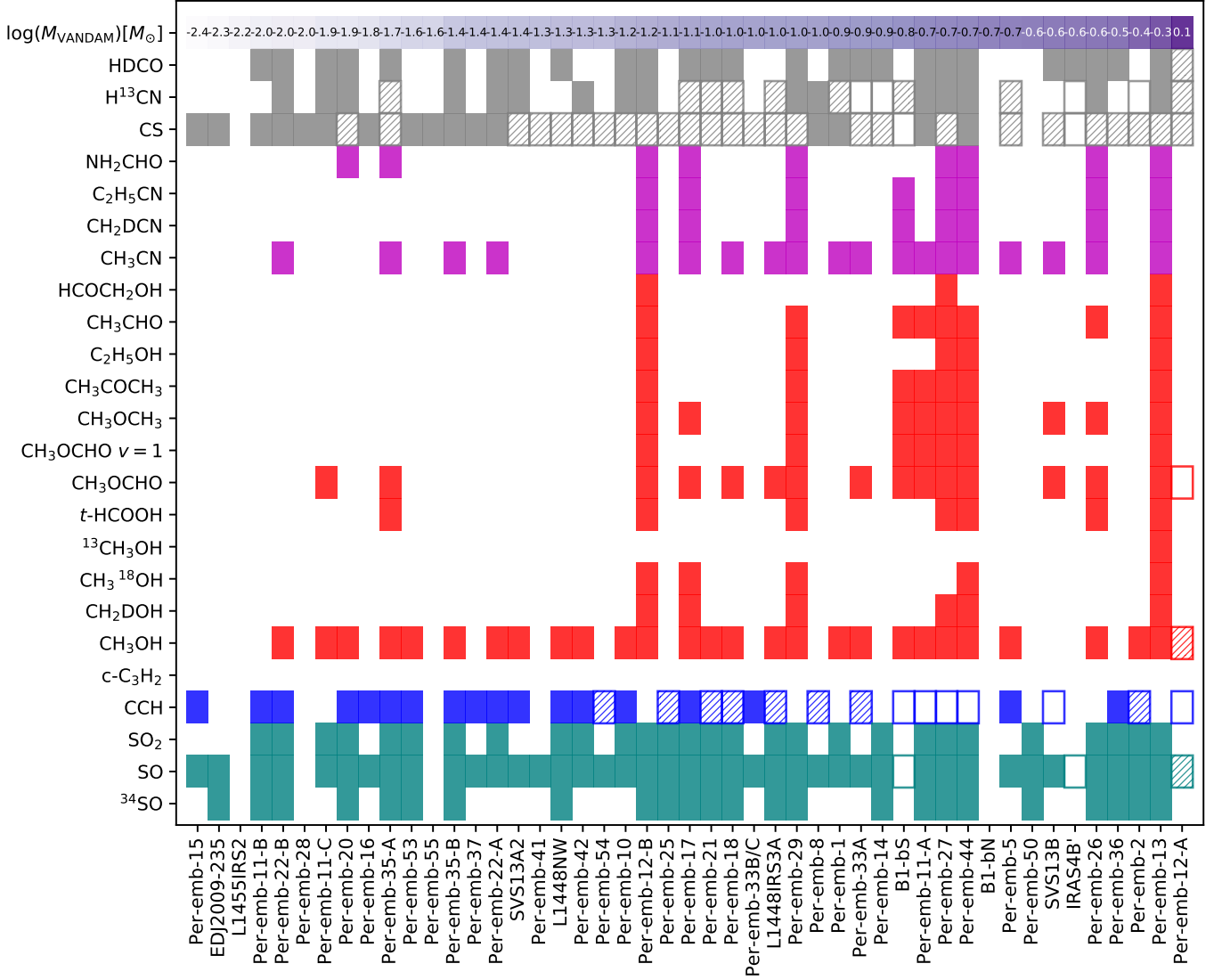


**Figure 2 (Cont.).** The same figure as Figure 2 but sorted by their mass derived from their 9 mm observations (Tychoniec et al. 2018).

- Unidentified lines at 246525 MHz and 244249 MHz.

*Per-emb-17*—

- Many line profiles exhibit a broad double-peaked profile, separated by  $\sim 5\text{--}6\text{ km s}^{-1}$ . *Per-emb-17* is a binary system unresolved by our observations. However, the channel maps suggest that the two components are likely to surrounding the southern source, *Per-emb-17-B*.
- The  $\text{CH}_3\text{OCHO}$  line at  $\sim 259343$  MHz may be optically thick.

*SVS13 A2*—

- Weak indication of the unidentified line at 246525 MHz, which has been detected in other sources.

*Per-emb-44*—

- Unidentified lines at 244248 MHz, 246219 MHz, 246254 MHz, 246344 MHz, 246389 MHz, 246434 MHz, 246525 MHz, 246838 MHz, 258268 MHz, 258271 MHz, and 262068–262070 MHz.

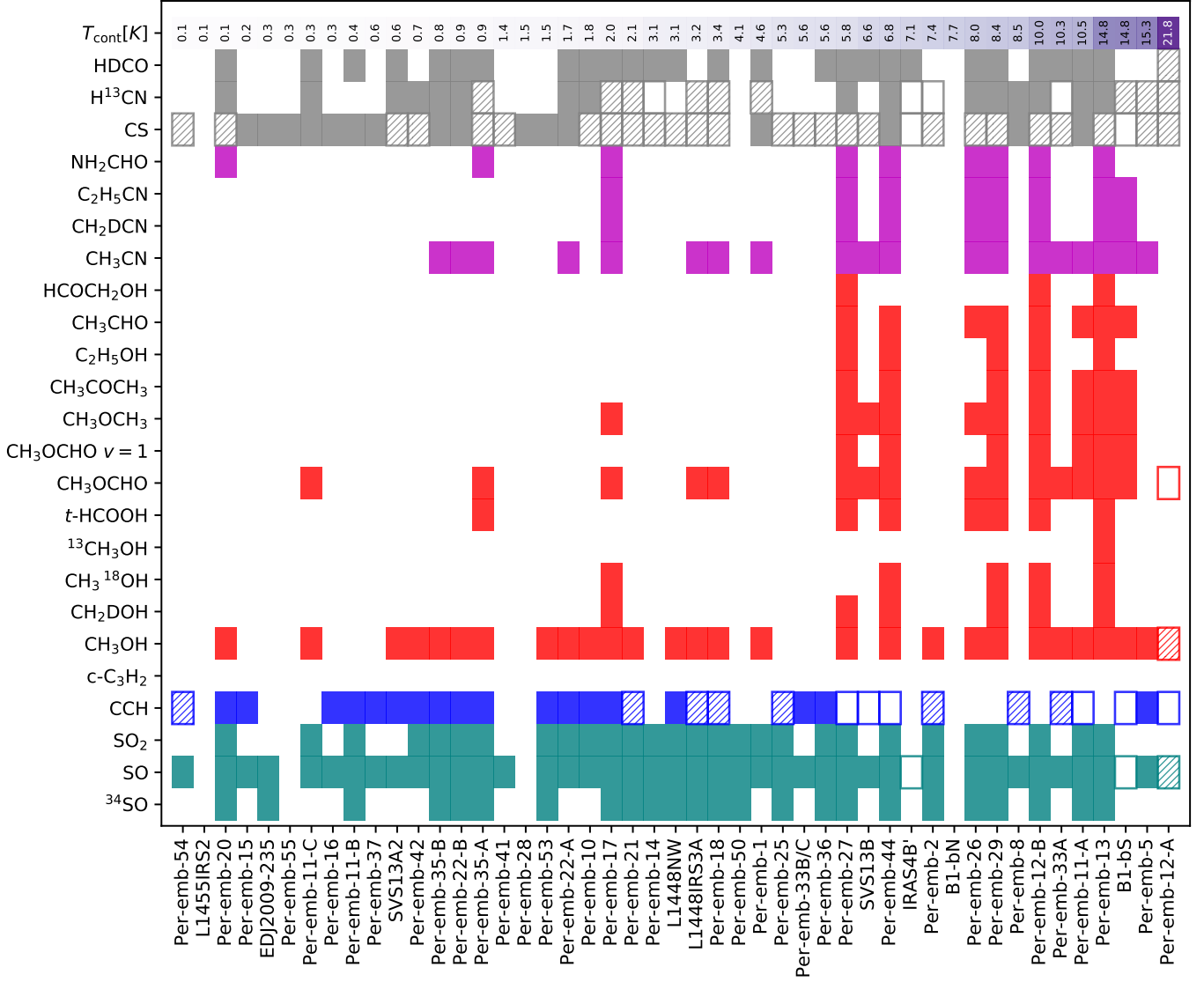


**Figure 2 (Cont.).** The same figure as Figure 2 but sorted by the continuum temperatures listed in Table 1.

- Higher temperatures ( $T_{\text{ex}} > 100$  K) provide better fittings. Probably should adopt the temperature fitted from  $\text{CH}_3\text{OCHO}$  (previous MCMC fitting suggests a temperature of 263 K).

*Per-emb-12-B*—

- Unidentified lines at 244248 MHz, 246254 MHz, 246314 MHz, 246322 MHz, 246389 MHz, 246434 MHz, 246525 MHz, 246696 MHz, 246838 MHz, 246873 MHz, 247082 MHz, 258268 MHz, 258271 MHz, and 262068-262070 MHz.

*Per-emb-12-A*—

- Strong absorption features detected across the spectra, CCH, SO,  $\text{H}^{13}\text{CN}$ , CS,  $\text{CH}_3\text{OH}$ , HDCO,  $\text{CH}_3\text{CN}$ , and  $\text{CH}_3\text{OCHO}$ .

*IRAS4B*—

- Spectra show no emission along with absorption at SO, CS, and  $\text{CH}_3\text{OH}$  lines.

*Per-emb-13*—

- The  $\text{CH}_3\text{OCHO}$  emission needs  $T_{\text{ex}} > 100$  K to have a good fit.



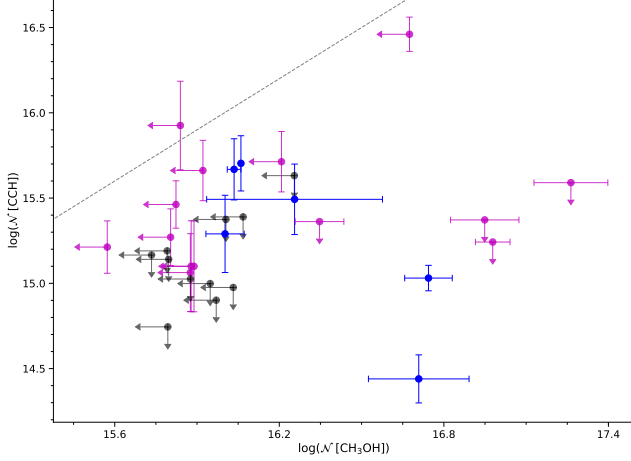


**Figure 3.** Correlation of the column densities of CCH and  $\text{CH}_3\text{OH}$  fitted from the PEACHES protostars. The sources where both molecules are detected are shown in black; the sources where only one molecule is detected are shown in magenta; finally, the sources where both molecules are not detected are shown in black for the corresponding upper limits.

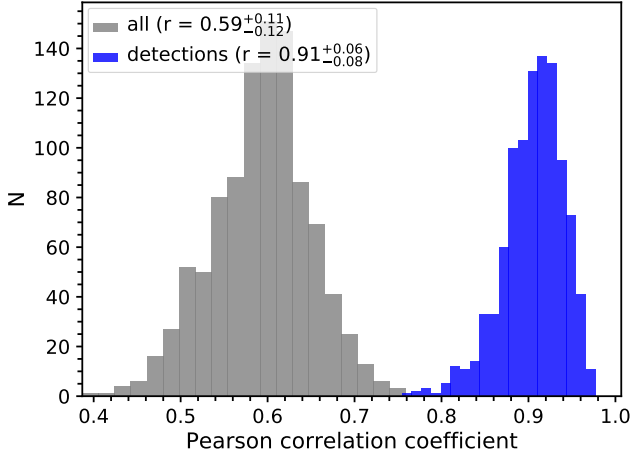


**Figure 4.** Distributions of Pearson's correlation coefficient from 10000 resamples drawn from detections + non-detections and only detections. The legend indicates the mean values of Pearson's  $r$  along with the range of the 95% credible interval as the associated uncertainties.

- All three  $\text{CH}_3\text{OH}$  lines are detected but two of them show clear sign of self-absorption, therefore, not ideal for fitting the excitation temperature.
- Unidentified lines at 244248 MHz, 246254 MHz, 246331 MHz, 246344 MHz, 246434 MHz, 246525 MHz, 246838 MHz, 246974 MHz, 247086 MHz, 257268 MHz, 257271 MHz, 259323 MHz, 259331 MHz, 262098 MHz, and 262109 MHz.
- The best-fitting model for  $^{13}\text{CH}_3\text{OH}$  lines overestimates the line width due to the weak and broad line at 247086 MHz.

*Per-emb-27—*

- All three  $\text{CH}_3\text{OH}$  lines are detected, but none of the temperature produce a good fit to all three lines, suggesting that some lines are optically thick. The intensities of the transitions at 243916 MHz and 261806 MHz are  $\sim 30$  K,

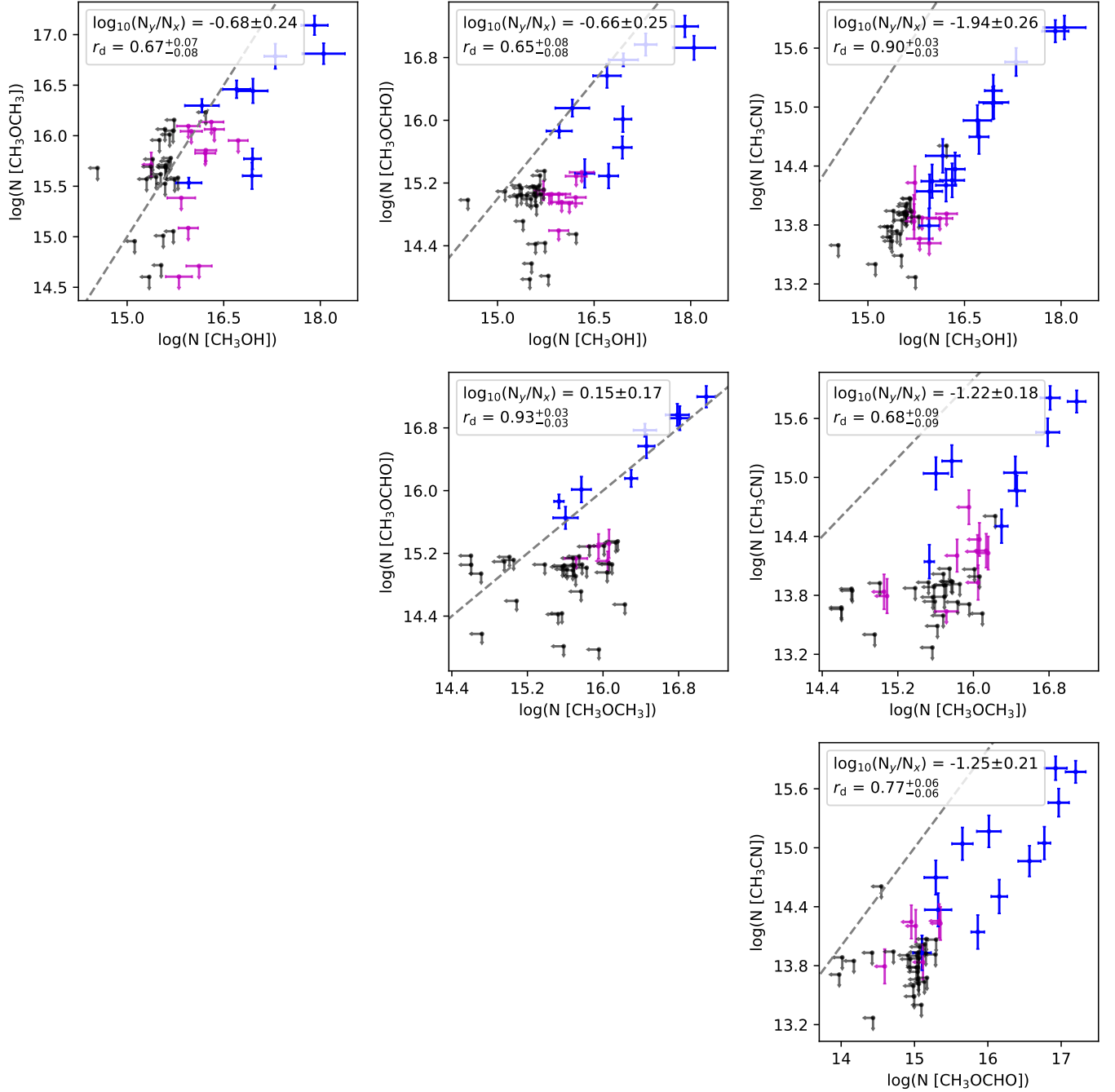


**Figure 5.** Corner plot of the correlations of the column densities between  $\text{CH}_3\text{OH}$ ,  $\text{CH}_3\text{CN}$ ,  $\text{CH}_3\text{OCHO}$ , and  $\text{CH}_3\text{OCH}_3$ . The color code follows that in Figure 3. The dashed line indicates equality. The legends indicate the Pearson's  $r$  for the detection-only sample ( $r_d$ ) and the logarithmic ratio of the two molecules ( $N_y/N_x$ ).

while the intensity at 246873 MHz is about 24 K. They seem to be optically thick. In comparison, the continuum brightness temperature is only 5.8 K.

- Unidentified lines at 244232 MHz, 244248 MHz, 246207 MHz, 246254 MHz, 246388 MHz, 246435 MHz, 246525 MHz, 246538 MHz, 246838 MHz, 246973 MHz, 247084 MHz, and 259330 MHz.
- The  $\text{CH}_3\text{OH}$  line at 243916 MHz and the SO lines become optically thick at 100 K.

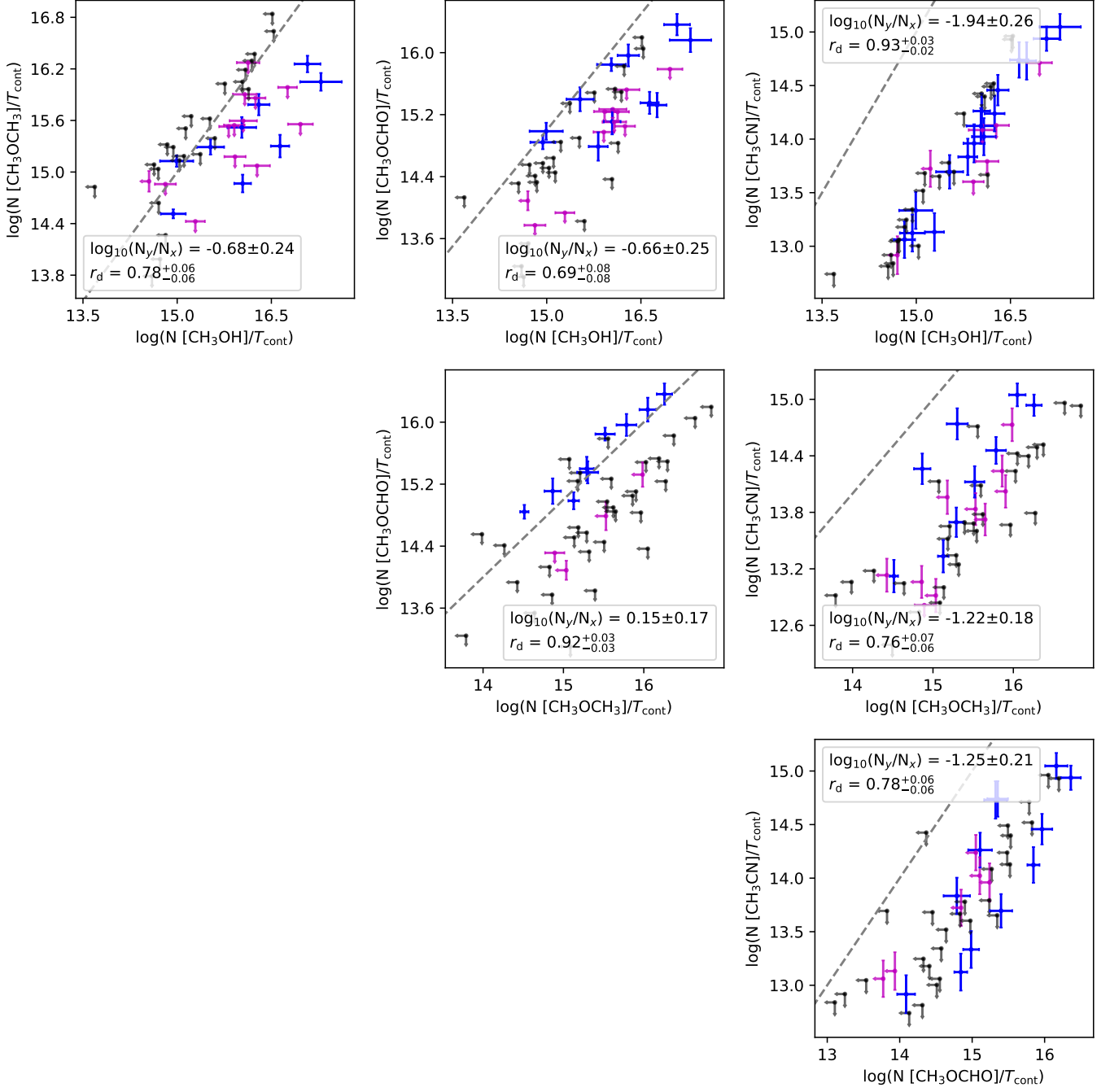


**Figure 5 (Cont.).** Corner plot of the correlations of the column densities normalized by the continuum brightness temperatures.

- Emission of  $\text{CH}_3\text{OH}$  is detected. However, the broad width and noisy spectra lead to a bad fit. The best-fitting model has the maximum line width allowed,  $3.5 \text{ km s}^{-1}$ .

*Per-emb-35-B*—

- The  $\text{CH}_3\text{OH}$  line at 243915 MHz has an S/N of 1.2, but hints the existence of  $\text{CH}_3\text{OH}$ .

*Per-emb-35-A*—

- The goodness of fitting for the  $\text{CH}_3\text{OH}$  lines is a strong function of temperature, suggesting that the  $\text{CH}_3\text{OH}$  lines can indicate the  $T_{\text{ex}}$ .

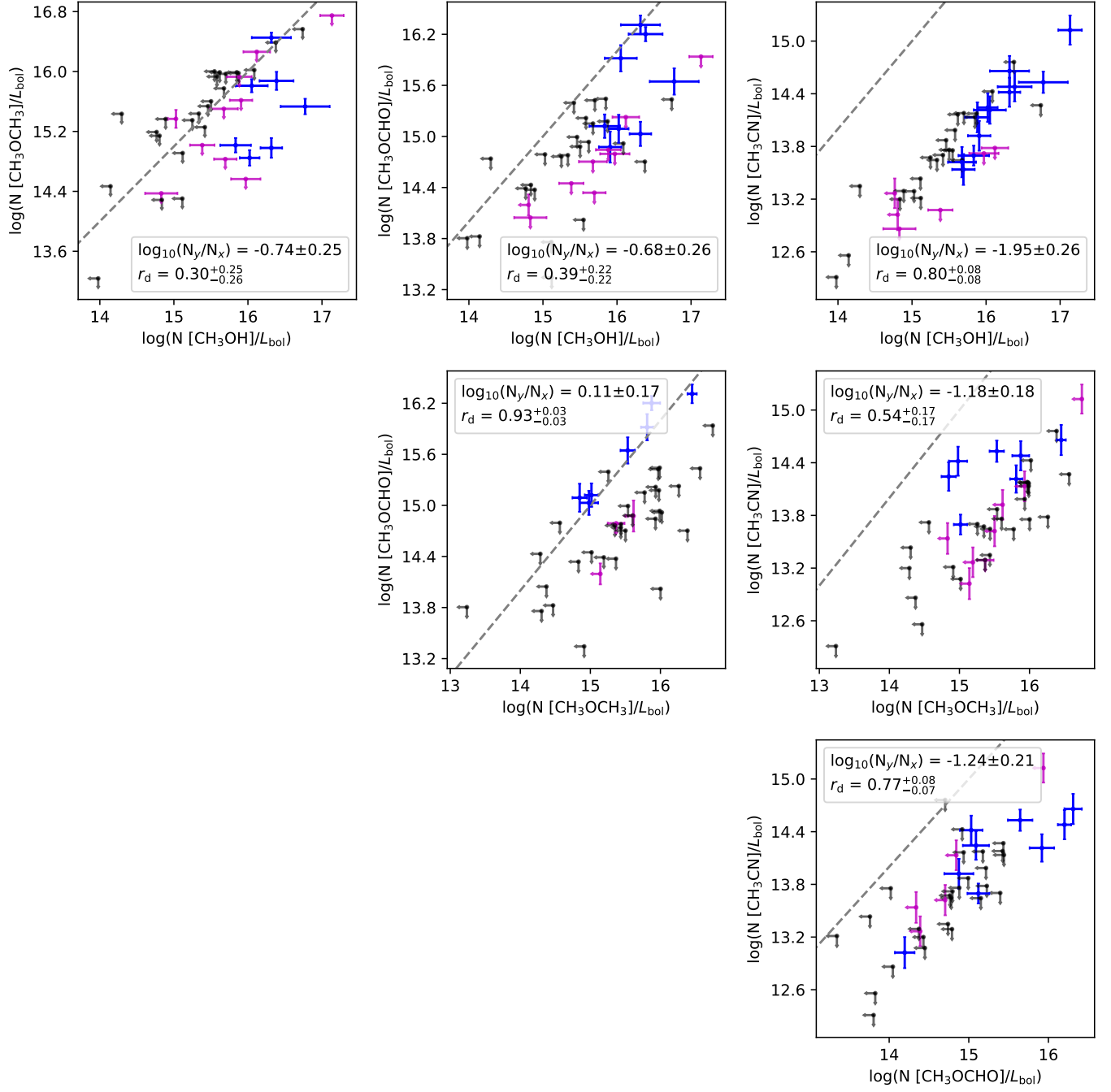


**Figure 5 (Cont.).** Corner plot of the correlations of the column densities normalized by the bolometric luminosities. A few close multiple sources, including Per-emb 12 A & B, Per-emb 35 A & B, and Per-emb 11 A & C, are excluded due to their poorly determined SEDs.

- The  $\text{CH}_3\text{OCHO}$  line at 259342 MHz has an S/N of 1.8, but hint the existence of  $\text{CH}_3\text{OCHO}$ .

*Per-emb-15—*

- All lines have only the blue-shifted emission, making them blue-asymmetric.

*Per-emb-18—*

- Many transitions of  $\text{CH}_3\text{OCHO}$  are tentatively detected; however, none of them has  $S/N > 3$ . Currently categorized as non-detection.

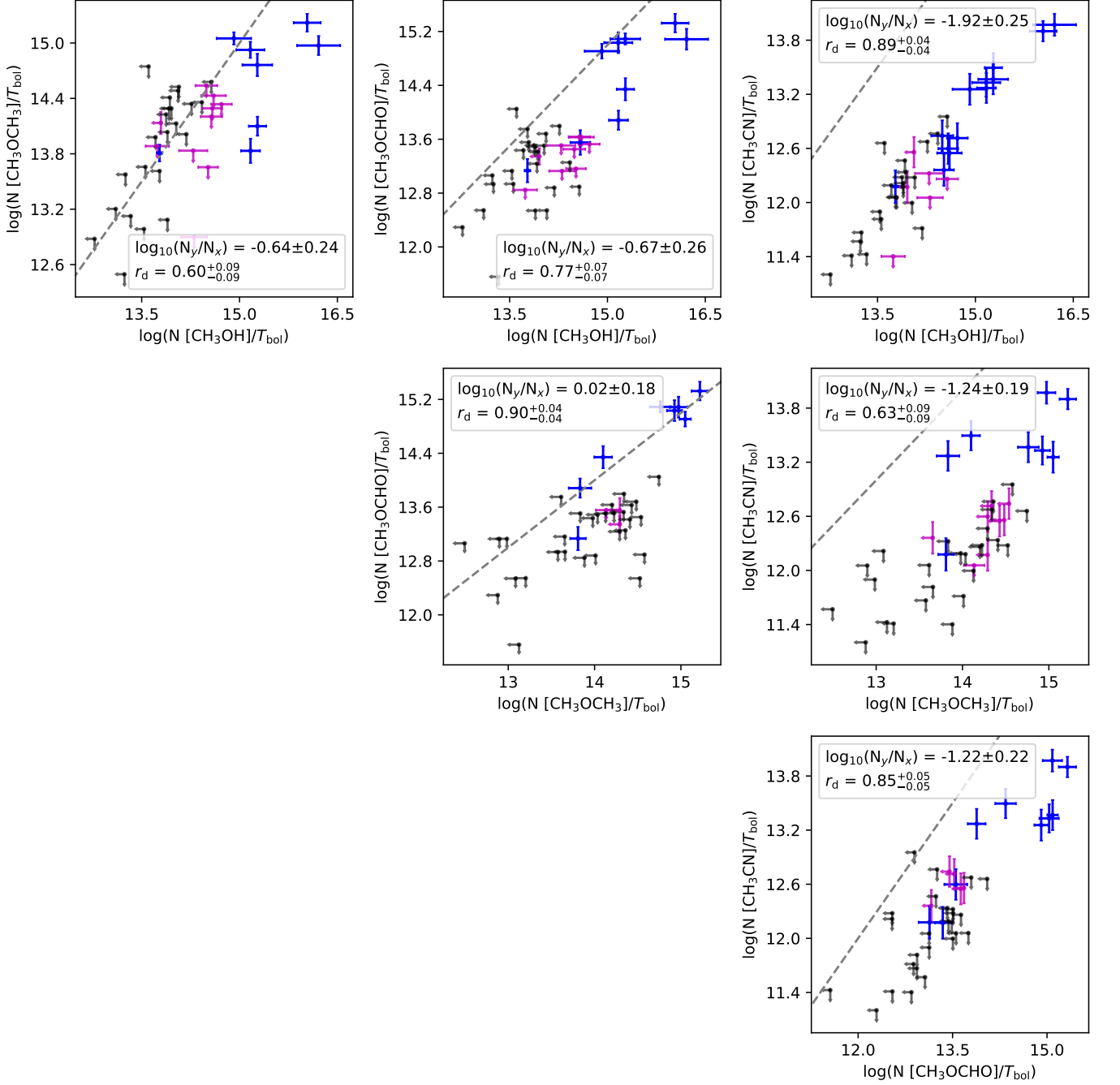


**Figure 5 (Cont.).** Corner plot of the correlations of the column densities are normalized by the bolometric temperatures. A few close multiple sources, including Per-emb 12 A & B, Per-emb 35 A & B, and Per-emb 11 A & C, are excluded due to their poorly determined SEDs.

*B1-bS*—

- Higher temperatures produce worse fittings to the  $\text{CH}_3\text{OCHO}$  lines. Previous MCMC fitting of the  $\text{CH}_3\text{OCHO}$  lines suggests a temperature of 58 K.
- The fitting of  $\text{CH}_3\text{OCH}_3$  is limited by the minimum line width of  $1.2 \text{ km s}^{-1}$ .
- Unidentified lines at 246027 MHz, 246099 MHz, 246143 MHz, 246192 MHz, 246525 MHz, 246674 MHz, and 2467320 MHz.

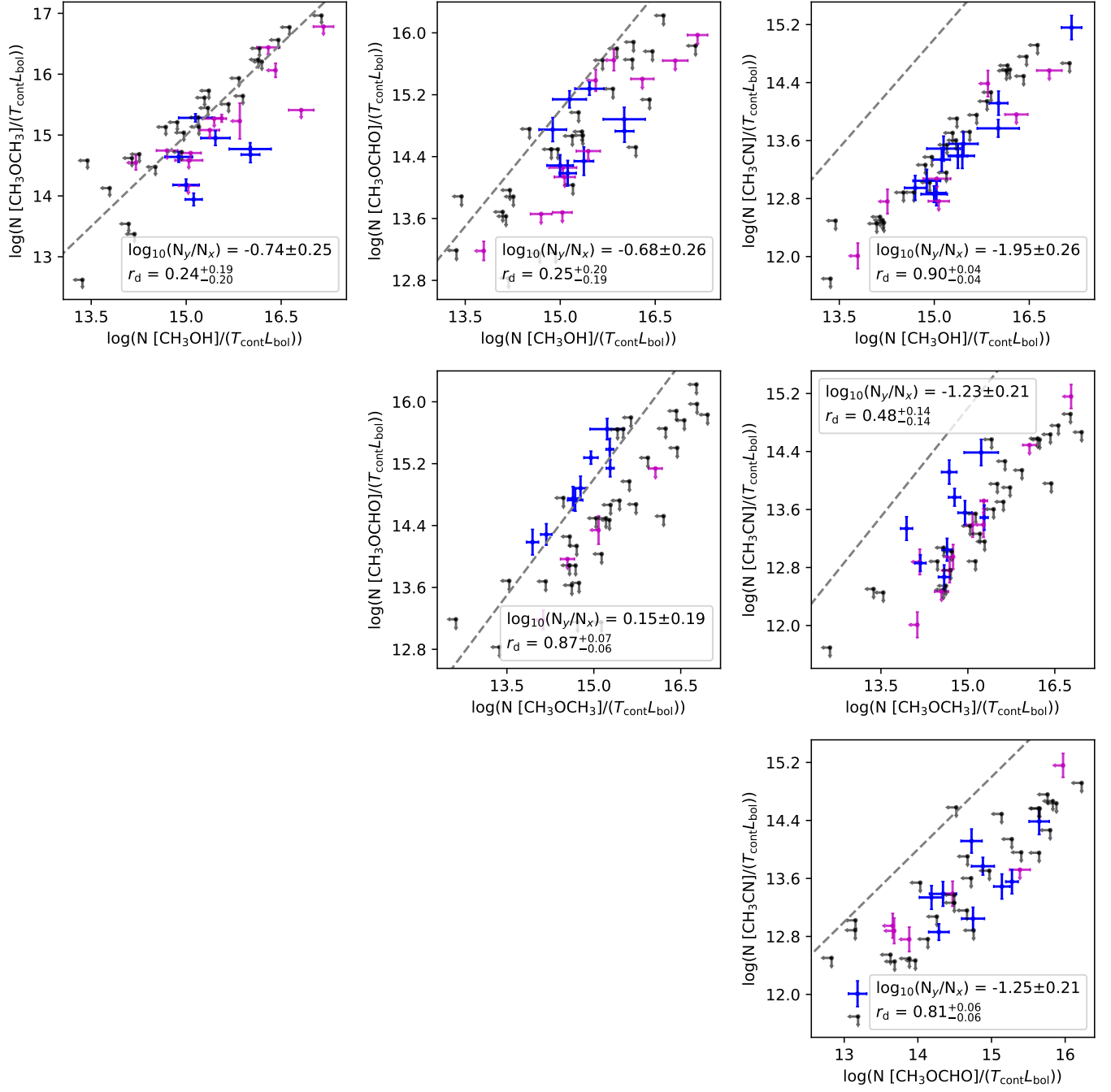


**Figure 5 (Cont.).** Corner plot of the correlations of the column densities are normalized by the continuum temperature and the bolometric luminosities. A few close multiple sources, including Per-emb 12 A & B, Per-emb 35 A & B, and Per-emb 11 A & C, are excluded due to their poorly determined SEDs.

- The  $\text{CH}_3\text{OCHO}$  lines around 258278 MHz and the  $\text{H}^{13}\text{CN}$  lines have a few dips within the line profile, suggesting absorption or just noisy spectra.

*Per-emb-29*—

- Only two  $\text{CH}_3\text{OH}$  lines are covered. Both lines have a strength of  $\sim 10$  K, suggesting optically thick.



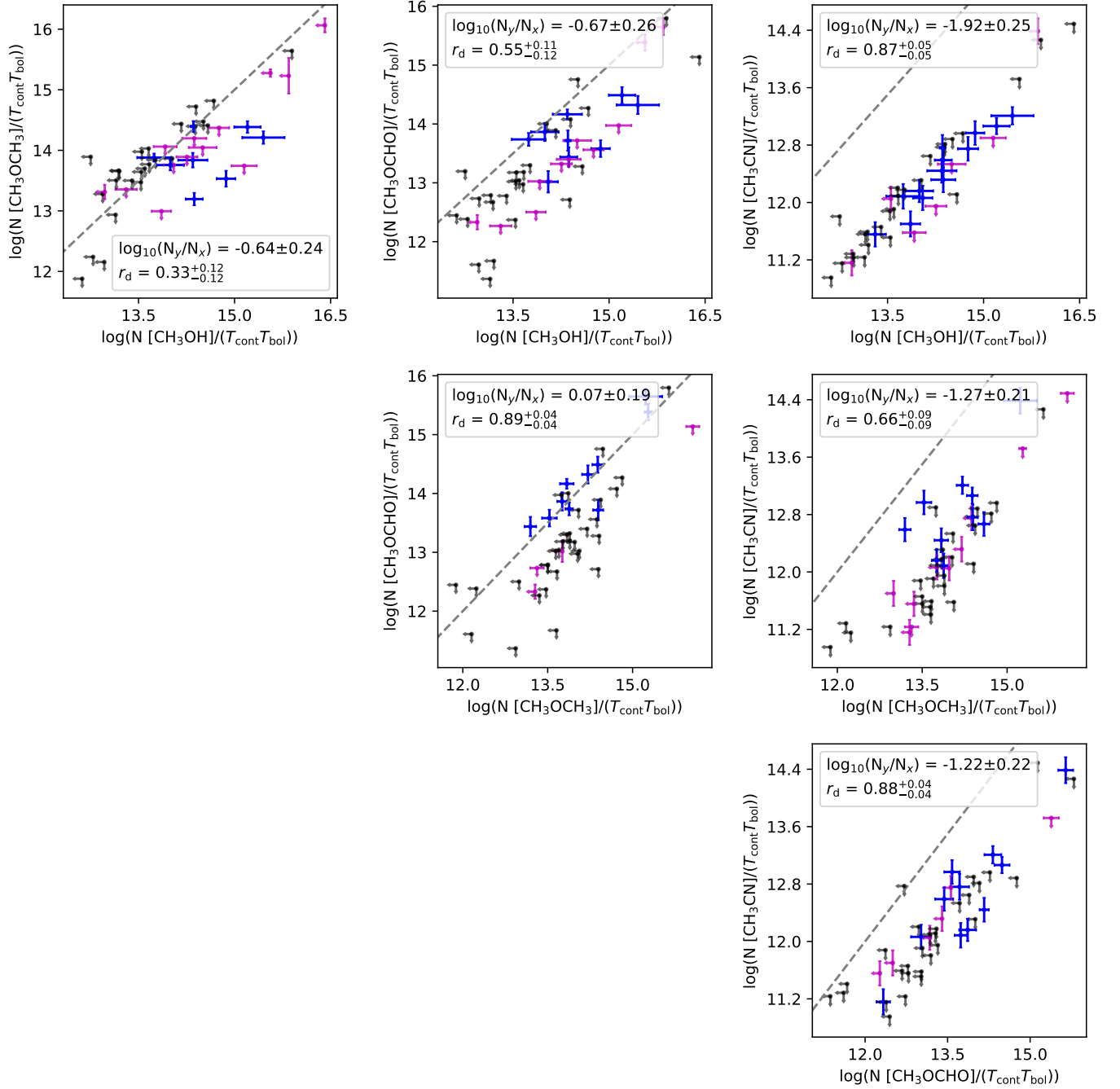


**Figure 5 (Cont.).** Corner plot of the correlations of the column densities are normalized by the continuum temperatures and the bolometric temperatures. A few close multiple sources, including Per-emb 12 A & B, Per-emb 35 A & B, and Per-emb 11 A & C, are excluded due to their poorly determined SEDs.

## REFERENCES

- Aikawa, Y. 2013, Chemical Reviews, 113, 8961, doi: [10.1021/cr4003193](https://doi.org/10.1021/cr4003193)
- Bottinelli, S., Ceccarelli, C., Lefloch, B., et al. 2004, ApJ, 615, 354, doi: [10.1086/423952](https://doi.org/10.1086/423952)
- Belloche, A., Maury, A. J., Maret, S., et al. 2020, A&A, 635, A198, doi: [10.1051/0004-6361/201937352](https://doi.org/10.1051/0004-6361/201937352)
- Carney, M. T., Yıldız, U. A., Mottram, J. C., et al. 2016, A&A, 586, A44, doi: [10.1051/0004-6361/201526308](https://doi.org/10.1051/0004-6361/201526308)

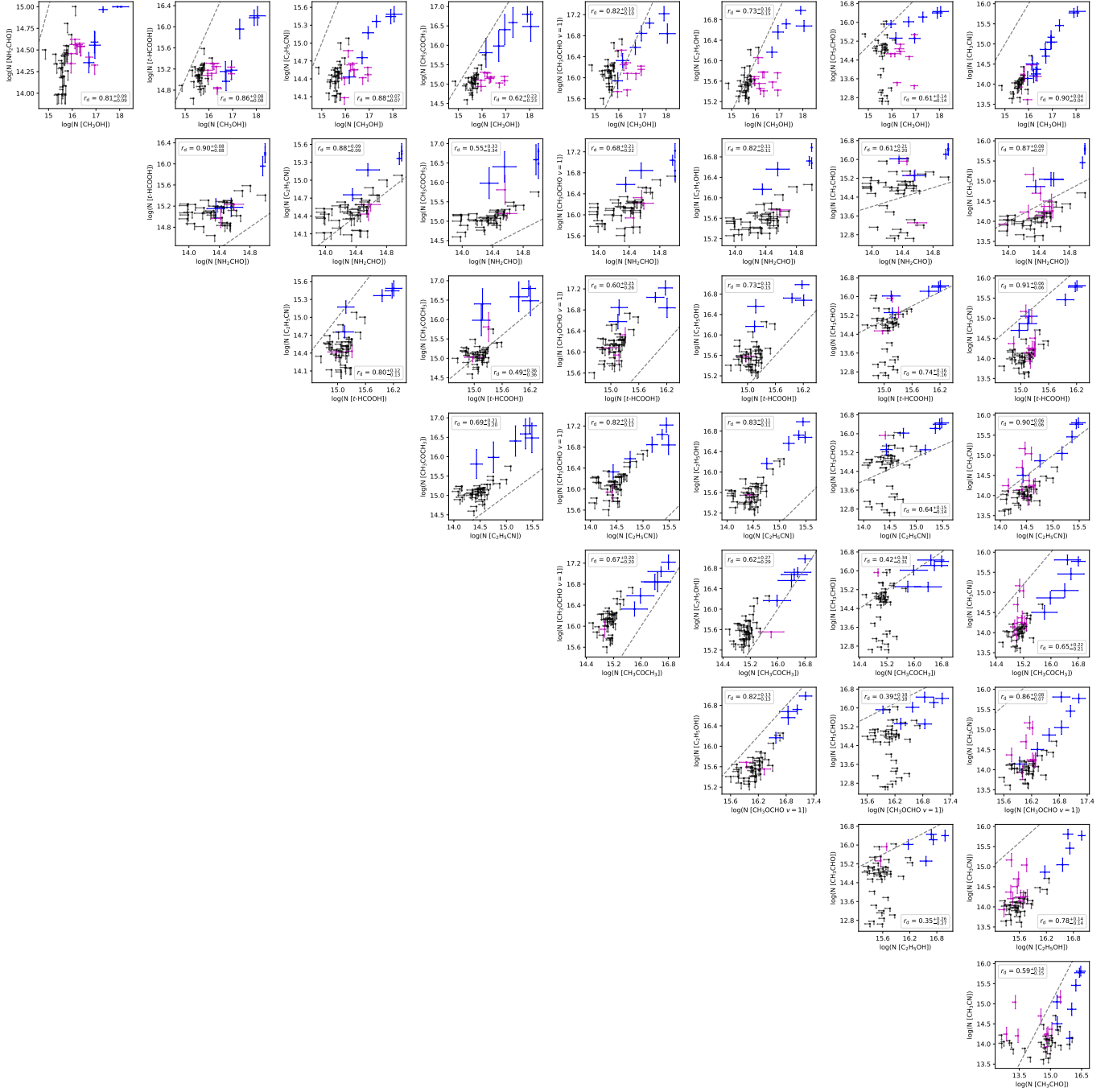


**Figure 6.** Corner plot of the correlations of the column densities between  $\text{CH}_3\text{OH}$ ,  $\text{CH}_3\text{CN}$ ,  $\text{CH}_3\text{CHO}$ ,  $\text{C}_2\text{H}_5\text{OH}$ ,  $\text{CH}_3\text{OCHO } v=1$ ,  $\text{CH}_3\text{COCH}_3$ ,  $\text{CH}_3\text{CH}_2\text{CN}$ ,  $t\text{-HCOOH}$ , and  $\text{NH}_2\text{CHO}$ . The legends are similar to Figure 5

Endres, C. P., Schlemmer, S., Schilke, P., Stutzki, J., & Müller, H. S. P. 2016, *Journal of Molecular Spectroscopy*, 327, 95, doi: [10.1016/j.jms.2016.03.005](https://doi.org/10.1016/j.jms.2016.03.005)

Graninger, D. M., Wilkins, O. H., & Öberg, K. I. 2016, *ApJ*, 833, 125, doi: [10.3847/1538-4357/833/1/125](https://doi.org/10.3847/1538-4357/833/1/125)

Herbst, E., & van Dishoeck, E. F. 2009, *ARA&A*, 47, 427, doi: [10.1146/annurev-astro-082708-101654](https://doi.org/10.1146/annurev-astro-082708-101654)

Higuchi, A. E., Sakai, N., Watanabe, Y., et al. 2018, *ApJS*, 236, 52, doi: [10.3847/1538-4365/aabfe9](https://doi.org/10.3847/1538-4365/aabfe9)

Imai, M., Oya, Y., Sakai, N., et al. 2019, *ApJL*, 873, L21, doi: [10.3847/2041-8213/ab0c20](https://doi.org/10.3847/2041-8213/ab0c20)

Imai, M., Sakai, N., Oya, Y., et al. 2016, *ApJL*, 830, L37, doi: [10.3847/2041-8205/830/2/L37](https://doi.org/10.3847/2041-8205/830/2/L37)

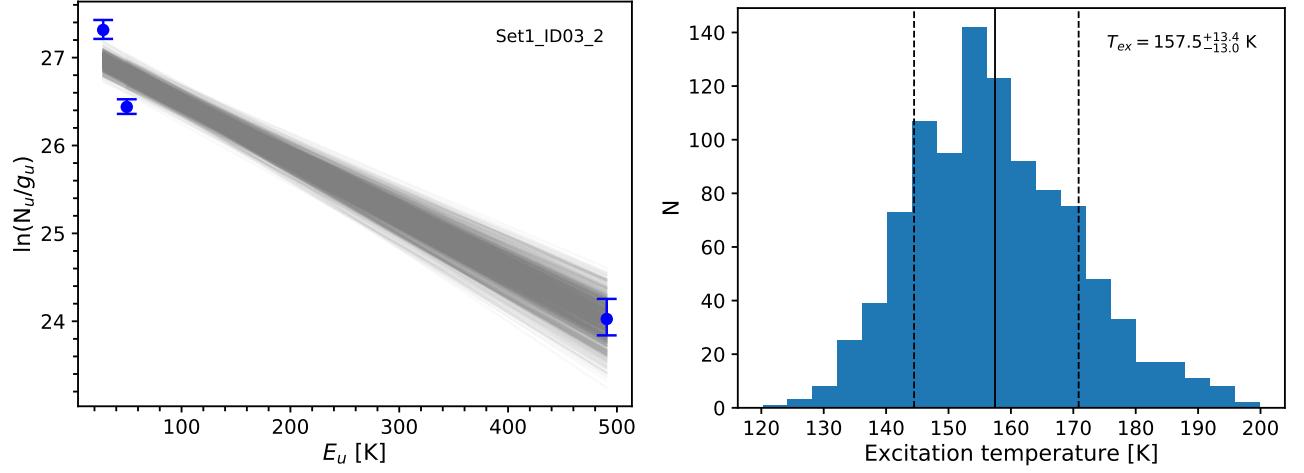


**Figure 7.** The methanol rotational diagram for Per-emb 22B and the fitted excitation temperature distribution using the bootstrapping method.

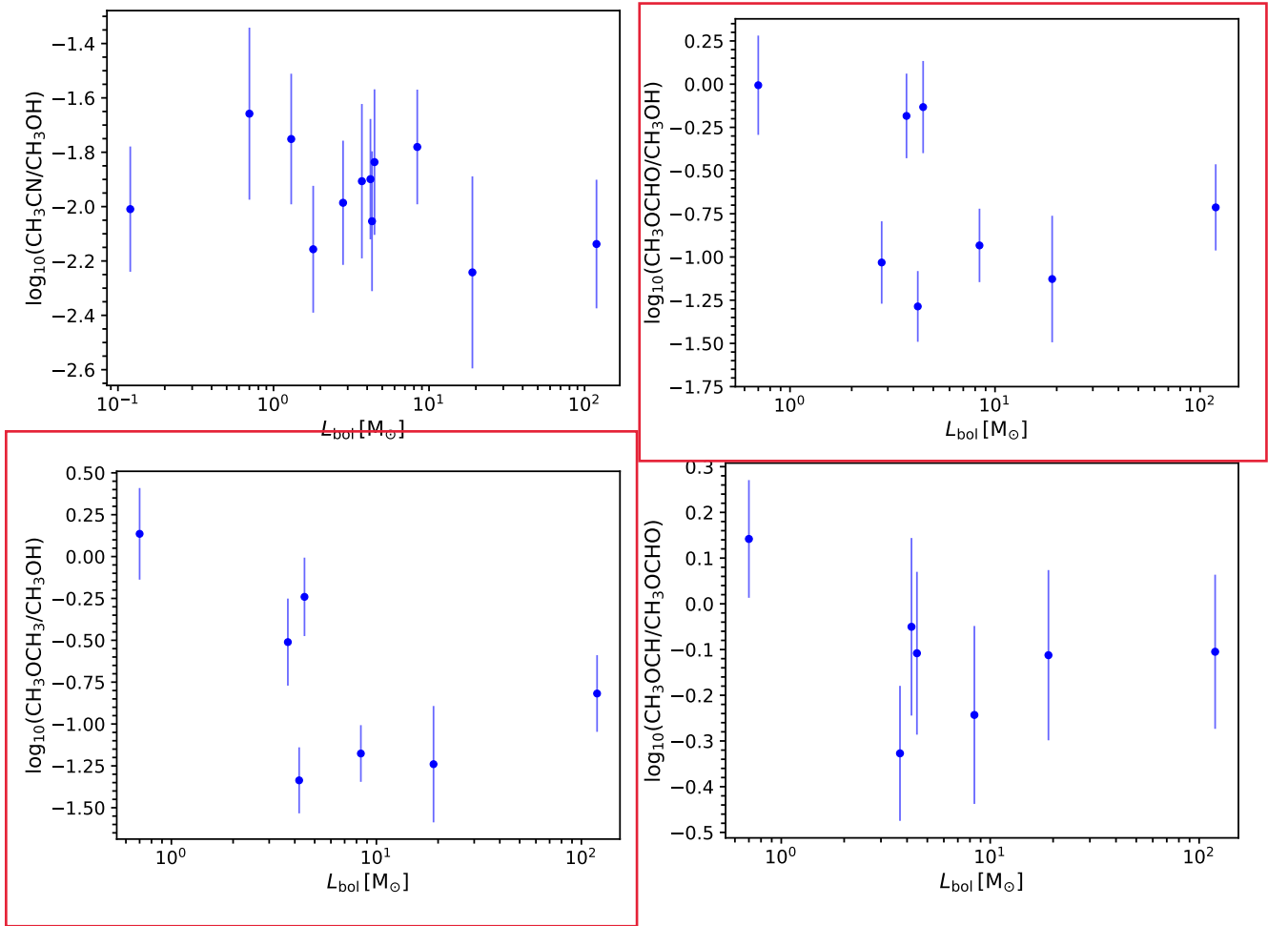


**Figure 8.** Ratios of molecules as a function of  $L_{bol}$ .

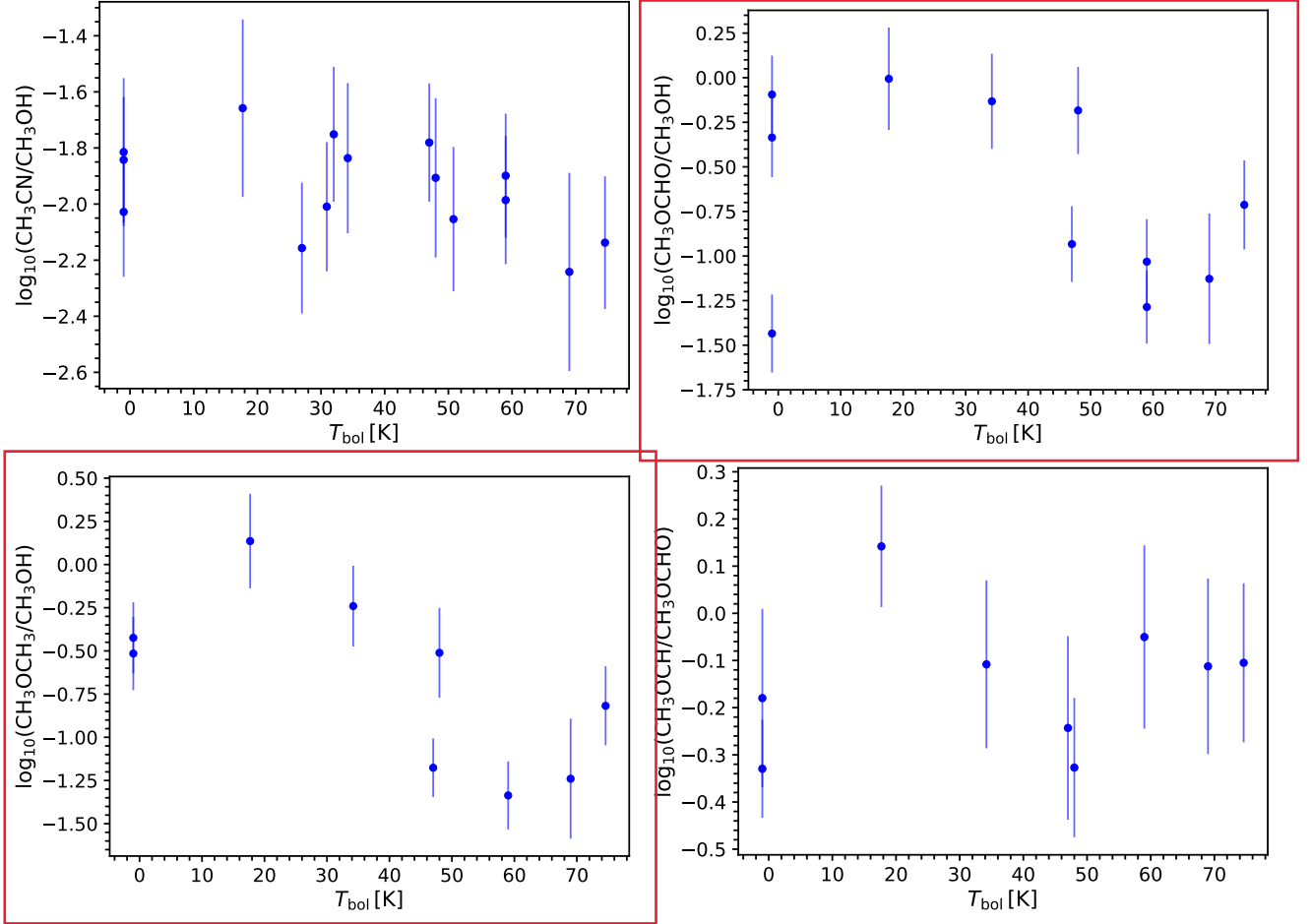


**Figure 9.** Ratios of molecules as a function of  $T_{\text{bol}}$ .

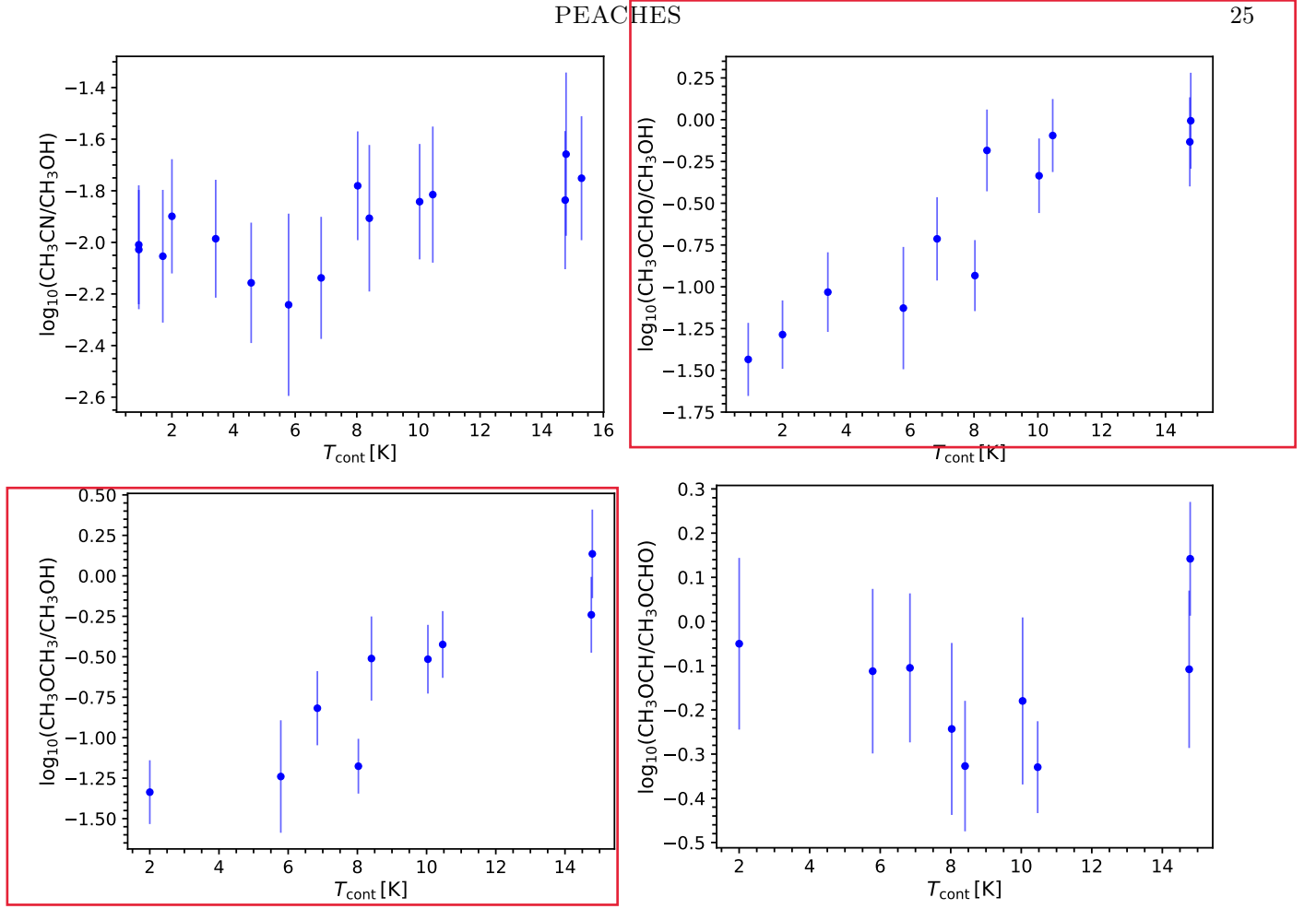


**Figure 10.** Ratios of molecules as a function of  $T_{\text{cont}}$ .

**Table 4.** Rotational Temperatures of Methanol

Source	$T_{\text{rot}}$
Per-emb 26	$120.1^{+2.6}_{-2.5}$ K
Per-emb 22 A	$182.4^{+11.2}_{-11.4}$ K
Per-emb 22 B	$157.5^{+13.4}_{-13.0}$ K
Per-emb 17	$173.9^{+1.8}_{-1.9}$ K
Per-emb 44	$197.5^{+0.3}_{-0.3}$ K
Per-emb 12 B	$194.0^{+0.8}_{-0.8}$ K
Per-emb 13	$208.6^{+3.9}_{-4.0}$ K
Per-emb 27	$195.8^{+0.4}_{-0.4}$ K
Per-emb 21	$151.0^{+14.6}_{-15.6}$ K
Per-emb 35 A	$145.1^{+3.7}_{-3.7}$ K
Per-emb 18	$395.7^{+30.7}_{-30.4}$ K
B1-bS	$241.7^{+11.7}_{-11.9}$ K
Per-emb 29	$227.7^{+3.2}_{-3.3}$ K

Jørgensen, J. K., van der Wiel, M. H. D., Coutens, A., et al. 2016, *A&A*, 595, A117, doi: [10.1051/0004-6361/201628648](https://doi.org/10.1051/0004-6361/201628648)

Lee, C.-F., Li, Z.-Y., Ho, P. T. P., et al. 2017, *ApJ*, 843, 27, doi: [10.3847/1538-4357/aa7757](https://doi.org/10.3847/1538-4357/aa7757)  
 McGuire, B. A. 2018, *ApJS*, 239, 17, doi: [10.3847/1538-4365/aae5d2](https://doi.org/10.3847/1538-4365/aae5d2)  
 Möller, T., Endres, C., & Schilke, P. 2017, *A&A*, 598, A7, doi: [10.1051/0004-6361/201527203](https://doi.org/10.1051/0004-6361/201527203)  
 Müller, H. S. P., Schlöder, F., Stutzki, J., & Winnewisser, G. 2005, *Journal of Molecular Structure*, 742, 215, doi: [10.1016/j.molstruc.2005.01.027](https://doi.org/10.1016/j.molstruc.2005.01.027)  
 Müller, H. S. P., Thorwirth, S., Roth, D. A., & Winnewisser, G. 2001, *A&A*, 370, L49, doi: [10.1051/0004-6361:20010367](https://doi.org/10.1051/0004-6361:20010367)  
 Oya, Y., Sakai, N., López-Sepulcre, A., et al. 2016, *ApJ*, 824, 88, doi: [10.3847/0004-637X/824/2/88](https://doi.org/10.3847/0004-637X/824/2/88)  
 Oya, Y., Sakai, N., Watanabe, Y., et al. 2017, *ApJ*, 837, 174, doi: [10.3847/1538-4357/aa6300](https://doi.org/10.3847/1538-4357/aa6300)  
 Pickett, H. M., Poynter, R. L., Cohen, E. A., et al. 1998, *JQSRT*, 60, 883, doi: [10.1016/S0022-4073\(98\)00091-0](https://doi.org/10.1016/S0022-4073(98)00091-0)  
 Sakai, N., Sakai, T., Hirota, T., Burton, M., & Yamamoto, S. 2009, *ApJ*, 697, 769, doi: [10.1088/0004-637X/697/1/769](https://doi.org/10.1088/0004-637X/697/1/769)

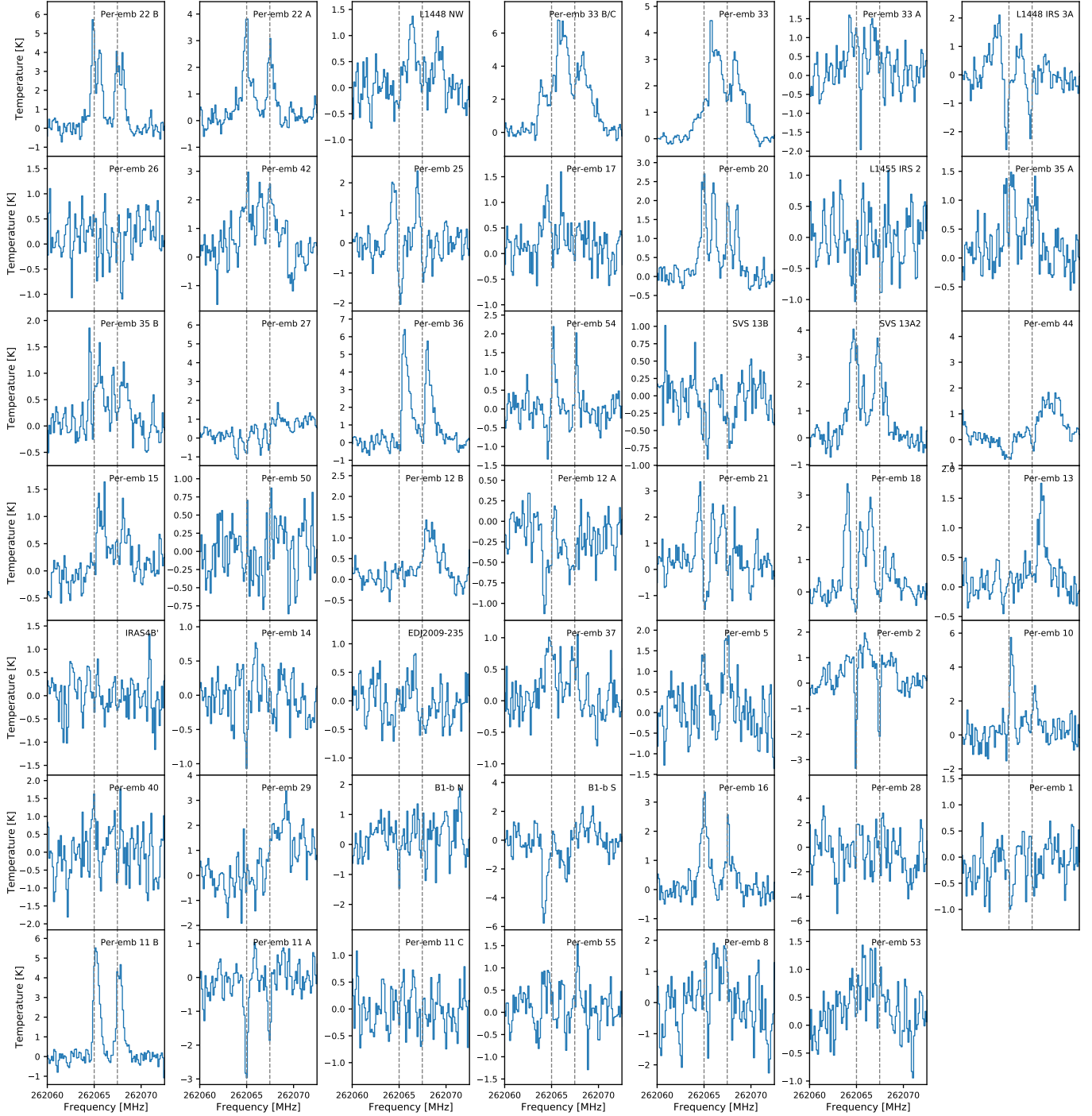


**Figure 11.** The CCH spectra of all PEACHES sources extracted from the continuum emission.

Sakai, N., Sakai, T., Hirota, T., & Yamamoto, S. 2010, *ApJ*, 722, 1633, doi: [10.1088/0004-637X/722/2/1633](https://doi.org/10.1088/0004-637X/722/2/1633)  
 Sakai, N., Sakai, T., Hirota, T., et al. 2014, *Nature*, 507, 78, doi: [10.1038/nature13000](https://doi.org/10.1038/nature13000)  
 Sakai, N., Oya, Y., López-Sepulcre, A., et al. 2016, *ApJL*, 820, L34, doi: [10.3847/2041-8205/820/2/L34](https://doi.org/10.3847/2041-8205/820/2/L34)  
 Stephens, I. W., Dunham, M. M., Myers, P. C., et al. 2018, *ApJS*, 237, 22, doi: [10.3847/1538-4365/aacda9](https://doi.org/10.3847/1538-4365/aacda9)

Stephens, I. W., Bourke, T. L., Dunham, M. M., et al. 2019, *ApJS*, 245, 21, doi: [10.3847/1538-4365/ab5181](https://doi.org/10.3847/1538-4365/ab5181)  
 Tychoniec, L., Tobin, J. J., Karska, A., et al. 2018, *ApJS*, 238, 19, doi: [10.3847/1538-4365/aaceae](https://doi.org/10.3847/1538-4365/aaceae)